International Journal of Multiphase Flow 150 (2022) 103891

Contents lists available at ScienceDirect

International Journal of Multiphase Flow

journal homepage: www.elsevier.com/locate/ijmulflow

Effects of isotropic and anisotropic turbulent structures over spray atomization in the near field

Marco Crialesi-Esposito [a,*], L.A. Gonzalez-Montero [b], F.J. Salvador [b]

[a] FLOW Centre, Department of Engineering Mechanics, KTH Royal Institute of Technology, Stockholm, Sweden
[b] CMT-Motores Térmicos, Universitat Politècnica de València, Spain

ARTICLE INFO

Keywords:
Spray
Turbulence
Primary atomization
Inflow boundary conditions

ABSTRACT

Sprays and atomization processes are extremely diffused both in nature and in industrial applications. In this paper we analyze the influence of the nozzle turbulence on primary atomization, focusing on the resulting turbulent field and atomization patterns in the Near Field (NF). In order to do so, a Synthetic Boundary Condition (SBC) and a Mapped Boundary Condition (MBC), producing respectively isotropic and anisotropic turbulent fields, have been generated as inflow conditions for the spray Direct Numerical Simulations (DNS). We present a specific methodology to ensure consistency on turbulence intensity and integral lengthscale between the two inflows. The analysis performed on the turbulent field (using one-point statistics and spectrum analysis) reveals a significantly stronger turbulent field generated by the inflow boundary conditions with anisotropic structures. While the increased turbulence field generated in the MBC case results in a higher number of droplets generated, the probability functions of both cases are extremely similar, leading to the non-obvious conclusion that the atomization patterns are only slightly affected by the inflow condition. These considerations are supported by the analysis of droplet size distributions, radial distribution functions, axial and radial distributions, highlighting extremely similar behaviors between the MBC and the SBC cases. Finally, these analyses and their computations are presented in detail, underlining how this type of point-process characterization shows interesting potential in future studies on sprays.

1. Introduction

Sprays are frequent physical processes in industrial applications and are easy to observe in many different fields. The main unknowns in these flows lie in how the droplets are generated (e.g. via which instability or mechanism), distributed (their position, size and velocity) and how they interact with each other. The analysis and determination of the main parameters describing droplets requires the understanding of the turbulence field developed in the region where atomization is occurring, which is usually non trivial. The most reliable way for analyzing sprays is therefore Direct Numerical Simulation (DNS), which allows to reach a sufficient resolution to resolve turbulence fluctuations even at the smallest scales, while providing a realistic representation of the droplets generated in the process. Among various numerical techniques, some of the most popular ones are the Volume of Fluid (VOF) method (e.g. Scardovelli and Zaleski (1999)), the Level-Set method from Sussman (1994) and the Front-Tracking method by Tryggvason et al. (2001). While the first two (considered as interface-capturing methods) are mass conserving (with some adjustments in case of the Level-Set method), the last is not and requires special treatments for abrupt topological changes such as the ones occurring during breakup.

The usage of DNS simulations allowed some important developments and findings lately. One of the first main contributions on primary atomization was provided by Shinjo and Umemura (2011, 2010), where a top-hat inlet velocity profile was used on a round spray to analyze the formation of the spray front and the related droplets generated. This rather simplistic setup limited the atomization and reduced the computational load, allowing to resolve up to 6 billion points in the simulation domain. Despite the inflow condition simplicity, some interesting results were harvested about the spray formation. In this paper, the same authors analyzed the effect of mesh size on artificial droplets, concluding that at least four cells per diameter in each direction were needed in order to consider a droplet as properly resolved. A more realistic (and complex) spray behavior was observed by Ménard et al. (2007), where the synthetic turbulence boundary condition (hereafter called Synthetic Boundary Condition, or SBC), developed by Klein et al. (2003), was used to simulate a diesel injector-like condition. The SBC calibration parameters were also studied in Salvador et al. (2018), where the usage of morphological analysis led to assess that larger turbulent structures generated within the nozzle lead to a significant

* Corresponding author.
E-mail address: marcoce@kth.se (M. Crialesi-Esposito).

https://doi.org/10.1016/j.ijmultiphaseflow.2021.103891
Received 2 December 2020; Received in revised form 8 November 2021; Accepted 12 November 2021
Available online 27 November 2021

modification of the spray intact-core-length, despite a reduced effect on the overall atomization pattern. A different approach in modeling the inlet boundary condition (or, in other terms, the outlet velocity profile of the nozzle) was used in Herrmann (2011) where a pipe flow DNS simulation output was stored and used as an input for the spray DNS simulation (this method is going to be called Mapped Boundary Condition or MBC hereafter). Here a significant change in the droplet distribution was noticed while refining the mesh grid.

The turbulence field produced in atomizing multiphase flows has also been analyzed in detail. Jarrahbashi and Sirignano (2014) studied the effects of vorticity in atomization prompted by aerodynamic shear, demonstrating how, in absence of external perturbations, counter-rotating hairpins are responsible for the formation and tear of liquid lobes and, ultimately, atomization. Ling et al. (2019) studied the behavior of a mixing layer and quantified its turbulence field by means of a turbulent kinetic energy budget, showing effects of mesh convergence as well as an interesting approach for calculating the energy spectra in the gas region. Hasslberger et al. (2019) used a topological analysis (based on the invariant of the velocity gradient tensor) to study the influence of the Reynolds number (Re) and Weber number (We) on the spray, concluding that among dimensionless numbers, Re is the one with the highest influence on the topological behavior.

Despite these many steps in understanding multiphase turbulence, liquid breakup and sprays, a quantitative estimation of the effects of turbulence on droplet generation is still missing (Desjardins et al., 2013). Furthermore, as DNS gets closer to represent real phenomena, a deeper understanding of how turbulence and gas–liquid interface are behaving when boundary conditions change is required. This is, in fact, one of the main goals of this paper. It is common practice, especially in lack of more complete information on the nozzle flow, to assume that homogeneous turbulence is developed at the nozzle outlet (Ménard et al., 2007; Hasslberger et al., 2019; Salvador et al., 2018) and that the integral length scale associated can be determined by means of literature on pipe flows DNS (e.g. Eggels et al. (2006)) or by experimental findings. On the other hand, a very different scenario is provided in wall flows, where anisotropy at large scales is often reported to be dominant and to affect the energy spectrum (del Álamo and Jiménez, 2003; Tsuji, 2003). Similar flow features are widely reported in nozzles, hence they deserve to be addressed.

An intuitive and qualitative understanding of the effects that different boundary conditions generate can be achieved by comparing the shape of the liquid external non-perturbed length. For example, the MBC case from Herrmann (2011) shows a significant development of liquid perturbation along the spray axial direction, while SBC cases, such as (Ménard et al., 2007; Hasslberger et al., 2019; Salvador et al., 2018), are showing more annular-like structures. Differences of liquid perturbations lead to the development of different shear stresses and breakup behavior, as observed by Jarrahbashi and Sirignano (2014), Salvador et al. (2018). On the other hand, no direct comparison criteria has ever been established between the different boundary conditions in MBC and SBC cases, hence a detailed comparison of their effects is overall unachievable.

This paper aims to address a fundamental aspect of primary atomization by finding an effective way to analyze the velocity field and the turbulence behavior while relating it to the droplets statistical characterization. The former will be analyzed by means of the energy cascade calculated using a pseudo-fluid approach (Torregrosa et al., 2020). For the latter a point-process approach will be used, as described in Subramaniam (2000) for a Klimontovich approach. While doing that, the comparison of a MBC and SBC cases will be performed. The data to be fed to the MBC case as Boundary Conditions (BC) will be generated using an Large Eddy Simulation (LES) of a periodic pipe flow and from its analysis the calibration parameter for the SBC case boundary conditions will be provided. For reasons that will later become evident, this will result in the comparison of how isotropic and anisotropic nozzle structures affect the breakup, providing a useful and novel insight on the interaction between large scale turbulence and liquid breakup. Simultaneously, this analysis will allow future studies to consider what are the benefits of using one of the two methods, what are the main differences and how this need to be accounted while studying the simulation results. The full description of the methodology used in this work will be provided in Section 2 for the DNS simulations and their setups (Sections 2.1 and 2.2) while more details on the LES, the post-processing and the analysis are available in Appendices A–C. Finally the whole analysis of the velocity field, the related turbulent spectrum and the droplet properties results will be presented in Section 3.

2. Methodologies

In Section 2.1 the DNS equations, the simulation setup and the physical parameters are presented. The reader should refer to Salvador et al. (2018) and Klein et al. (2003) for a more accurate description of the boundary condition used in the SBC case. In this method, the turbulence field (for the isotropic case) is described by I (turbulent intensity) and L (turbulent length scale). The computation of these parameters from the LES simulation will be presented in Section 2.2. More information on the post-processing methodology and the LES simulation are available in the Appendices.

2.1. Methodology description for the DNS simulation

The DNS simulations were performed using the open-source code ParisSimulator, which full features and algorithms description can be found in literature (Aniszewski et al., 2021, 2019; Tryggvason et al., 2011; Ling et al., 2015). Briefly, the code simulates a multiphase incompressible flow over a fixed Cartesian mesh using the following conservation equations:

$$\nabla \cdot \mathbf{u} = 0 \tag{1a}$$

$$\rho\left(\frac{\partial \mathbf{u}}{\partial t} + \mathbf{u}\cdot\nabla\mathbf{u}\right) = -\nabla p + \nabla\cdot\left[\mu(\nabla\mathbf{u} + \nabla\mathbf{u}^T)\right] + \sigma\kappa\delta_s\mathbf{n} \tag{1b}$$

$$\frac{\partial C}{\partial t} + u\cdot\nabla C = 0. \tag{1c}$$

In the above equations, $\mathbf{u}$ represents the velocity field, which due to the incompressibility hypothesis results to be divergence free, as stated in Eq. (1a). The pressure is represented by p, while the properties ρ and μ are respectively the fluid density and dynamic viscosity. The third term on the right hand side of Eq. (1b) represents the contribution provided by the surface tension forces at the interface. A Dirac distribution function δ_s is used to concentrate this force on the liquid surface. Consequently, σ is the surface tension, $\mathbf{n}$ is the surface normal and κ is the liquid surface curvature.

Eq. (1c) is the advection of the color function C which is used to compute the local value of density and viscosity and for detecting the liquid surface position. The local value of ρ and μ is computed in Eq. (1b) by arithmetic mean:

$$\rho = C\rho_l + (1-C)\rho_g \tag{2a}$$

$$\mu = C\mu_l + (1-C)\mu_g \tag{2b}$$

where the subscripts l and g indicate the liquid and the gas phase.

The Chorin projection method (Chorin, 1968) is used to solve the velocity field, while the resulting variable coefficient Poisson equation is solved using a iterative Gauss–Seidel algorithm. The spatial discretization of the momentum advection is performed using the QUICK algorithm (Leonard, 1979), while the diffusive flux is solved using a second-order central scheme. Finally the advection equation for the color function is solved through the VOF method (Scardovelli and

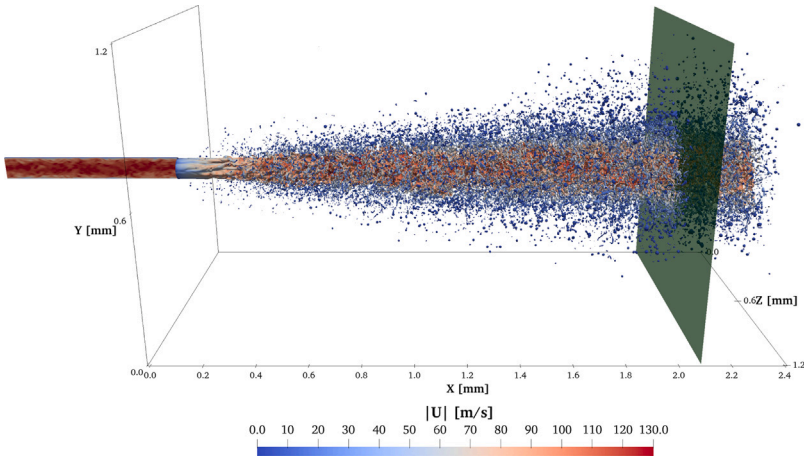

Fig. 1. Simulation sketch. On the left side (outside of the simulation domain) a slice from the LES flow used to generate the MBC inflow. Within the domain, a VOF render of the spray, colored by the velocity magnitude. In green, the plane over which turbulence statistics are collected. (For interpretation of the references to color in this figure legend, the reader is referred to the web version of this article.)

Zaleski, 1999). The advection of the interface is performed using a modified version of the PLIC algorithm, called the Calcul d'Interface Affine par Morceaux (CIAM). The surface tension contribution is computed using a Continuous Surface Forces approach and the height-function method (in its version by Popinet (2009)) for computing the curvature. Further details on the solver and the numerical schemes may be found in Tryggvason et al. (2011) and Ling et al. (2019).

The fluid properties and flow setup are the same for both the nozzle flow LES (required for the MBC case) and the DNS simulations and are reported in Table 1 where $\langle U \rangle$ is the liquid inlet average velocity, D_n is the nozzle diameter and Re_b is the Reynolds bulk number, computed using the average injection velocity and liquid properties. Fig. 1 shows a sketch of the simulation domain. Outside the domain on the left, we show a plane colored by the velocity module from the LES simulation used to generate the MBC inflow (more details about the procedure are available in Appendix A). On the right, a green plane shows the subdomain where turbulence statistics are collected (see Appendix C for more details).

The simulation setup, as well as the domain design is reported in Table 2. Being the mesh Cartesian, dx is the cell size, equal in each direction, dt is the time-step, l_i is the domain length in the ith direction. Finally, the simulation time are reported as T_t and T_{ss} where the former is the transient time and the latter is the statistically stationary time. T_t can be defined as the time required by the spray to reach the end of the domain and stabilize, while T_{ss} is the time over which the statistical analysis is performed. The total simulation time is $T_{tot} = T_t + T_{ss}$. A clarification is required in order to understand how these intervals were determined and what are their implications on the simulation analysis. In the dense region, no correlations are available to estimate the axial velocity loss. For this reason, it is necessary to define a quantity that can be used to describe the specific transient time and the statistical stationary time of the flow analysis in object. Therefore, we defined the number of washouts $N_w = \langle U \rangle T_i / l_x$ as the total number of times that a liquid parcel, injected into the domain with a velocity $\langle U \rangle$, will travel for a length l_x in the streamwise direction during the total time interval T_i considered. Due to the axial velocity losses discussed before, the number of washouts for the transient has to be greater than one and in this case, it has been set to 1.7, while for the statistical stationary part, we set $N_w \approx 11$. It should also be noted that, as discussed by the authors in Salvador et al. (2018), the real penetration is affected by the centerline velocity, hence N_w could also result into higher values (and therefore more accurate statistics). To the best of the authors knowledge, this represents the longest temporal statistical analysis performed over sprays (Ling et al., 2019). Finally, it is well known that droplet's generation is an inherently transient phenomena.

Table 1
Physical simulation properties for the case studied.

Re_b	ρ_l	ρ_g	μ_l	μ_g	σ	$\langle U \rangle$	D_n
5037	750	22.8	$1.34 \cdot 10^{-3}$	$1.85 \cdot 10^{-5}$	$2.53 \cdot 10^{-2}$	100	90
–	kg/m^3	kg/m^3	Pa s	Pa s	N/m	m/s	μm

Table 2
Simulations setup.

dx	dt	l_x	$l_{y,z}$	T_t	T_{ss}
2.34	4.0	2.4	1.2	0.04	0.26
μm	ns	mm	mm	ms	ms

As droplets can accumulate in the domain upon being generated, a proper statistically-stationary state for droplets generation is hardly reachable. Hence, statistical stationary in this work has to be intended as referred to kinematic properties. As it will be shown later, after the initial transient, droplets generation rate decreases significantly, hence statistics become meaningful also for droplets.

A remark should be made about the choice of dx. As, among the prerequisites of DNS simulations is the solution of all the energy scales up to the Kolmogorov scale, an a-priori estimation of η was performed. According to literature (e.g. Pope (2001)) a rough estimation for the Kolmogorov scale can be given by $\eta \sim L Re_L^{-3/4}$ (Hasslberger et al., 2019). By using an approximation for the turbulent lengthscale $L \sim D_n$ (a normal assumption in spray simulations), and estimating u_{rms} from Salvador et al. (2018) gives $\eta \approx 1.15\,\mu$m. Due to η estimation, and consistently with what proposed in literature for recent similar works (e.g. Ling et al. (2019) and Hasslberger et al. (2019)) the mesh size has been taken roughly twice the size of η, respecting the criteria of $dx/\eta \leq 2.1$ (Pope, 2001; Ling et al., 2019). This is a fair compromise for computing times (half the mesh size corresponds to 16 times the computation time in Cartesian meshes) and the amount of required statistical data while still granting reliable results. On the other hand, it will be shown in Section 3.2 that a local estimation of η demonstrates that an a-priori determination of this parameter, in line with literature approaches, is over-estimating the Kolmogorov scale. The implications will be discussed later in the paper.

2.2. Turbulent intensity and lengthscale extraction from the pipe LES simulation

In order to produce the information for the inflow velocity profiles of the MBC case, we performed a single-phase LES simulation of a

cylindrical pipe, of diameter D_n and length $8D_n$, for the same Re_b of the DNS simulation. The simulation is performed using periodic boundary conditions along the streamwise direction and by adding an imposed pressure gradient source term to maintain the flow at Re_b=5037. More details are available in Appendix A.

The parameters I and L, used for the synthetic turbulent filter in the SBC case, can be computed from the LES results. Their derivation has been made rigorously in this case, as it is important to limit the differences between SBC and MBC cases only to quantifiable causes. The integral lengthscale is defined as the largest scale in the flow. The same definition can be applied to the so-called turbulent lengthscale L, which is the same in nature. The equation defining L can be found considering the azimuthal direction as the homogeneous one (i.e. equidistant from the wall) for the pipe flow. The result is:

$$L(r,t) = \int_0^{2\pi} f_{11}(r,\delta\theta,t) r d(\delta\theta) \tag{3}$$

where r is the radial distance from the pipe center (equal to $D_n/2$ at the wall), θ is the azimuthal coordinate and f_{11} is the dimensionless autocorrelation function. As known from literature (Pope, 2001), for wall-bounded flows, r is the direction of heterogeneous turbulence intensity (as demonstrated in Fig. A.18(*b*)) while $\delta\theta$ is the angular increment vector in the direction along which the turbulence is statistically homogeneous. Therefore, fixing r and varying θ we can find a number of locations (finite in our discrete analysis) where the turbulence behaves similarly over time. In other words, we can identify θ as an homogeneous direction. This consideration implies that if we integrate over θ, a time-average of $f_{11}(r,\theta,t)$ provides smooth and convergent statistics. Finally, the autocorrelation function for the axial velocity component is used.

The calculation of the dimensionless autocorrelation function can be done by considering that the signal is indeed periodic when sampled over θ, hence the first and the last value of the autocorrelation need to be identical when the total autocorrelation length is 2π. Furthermore, being the signal periodic it is always possible to compute the product $u(\theta)u(\theta+\delta\theta)$ with $\delta\theta \in [0, 2\pi[$ simply by concatenating the signal of sample length N_s twice and compute the autocorrelation only over N_s elements (Torregrosa et al., 2020). Therefore, the formal definition of the dimensionless autocorrelation function is:

$$f_{11}(r,\delta\theta,t) = \frac{\langle u(r,\theta,t)u(r,\theta+\delta\theta,t)\rangle}{\langle u(r,\theta,t)^2\rangle} \tag{4}$$

The computation of Eqs. (3) and (4) provides the result showed in Fig. 2(*a*), where the dimensionless autocorrelation functions for different radial positions are shown as a function of $\xi = \theta/2\pi$. This figure also shows that autocorrelations $f_{11}(r,\theta)$ for small values of r does not reach decorrelation (i.e. $f_{11}(r,\theta) > 0$ for any θ). This is a clear indicator of the presence of numerous large structures close to the pipe centerline.

Applying Eq. (3) on $f_{11}(r)$ leads to the results in Fig. 2(*b*). The function $L(r)$ is finally averaged to produce a single scalar usable for the SBC case. The result produces a value for L of 9.23 μm, which corresponds to 10.25% of the nozzle diameter, D_n. It is important to remember that the integral lengthscale computed here is not the one we used in Section 2.1 to estimate the Kolmogorov scale. In fact, as the flow exits the nozzle, the problem changes significantly and the largest scale increases. The value of L computed here is the integral lengthscale within the nozzle, which is the largest scale developed in the confined flow.

The definition of I mostly used in CFD is:

$$I = \frac{|u_{rms}|}{|\langle U\rangle|} = 0.16 Re_b^{-1/8} \tag{5}$$

where u_{rms} is the root-mean-squared component of the velocity, accounting for all components. The last formulation of Eq. (5) is the one mostly used in RANS/LES simulations and, in this case (using data from Table 1) gives 5.51%. On the other hand the formal definition was used (first formulation in Eq. (5)) and averaged over the whole domain, with a result of 5.88%, which is the value that was ultimately used in the SBC case.

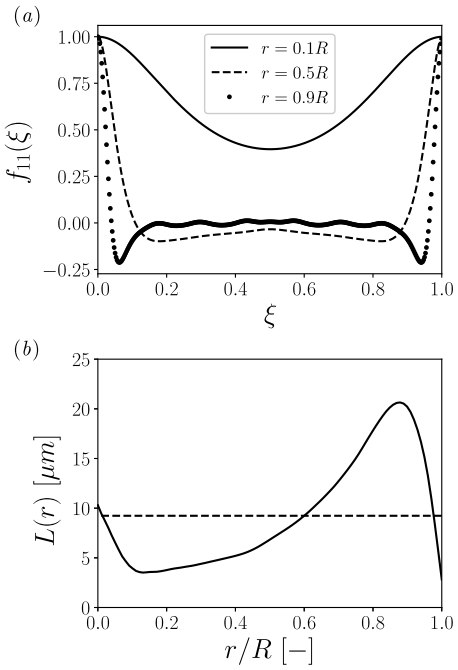

Fig. 2. Results of LES analysis. Panel (*a*): Autocorrelation for the LES simulation of pipe flow. Panel (*b*): Turbulent integral lengthscale as a function of the radial position in the pipe flow.

3. Analysis

In this section, the comparison between the MBC and the SBC cases will be performed by analyzing their one-point statistics in Section 3.1. The determination of space-varying average turbulence properties, as the local Kolmogorov scale and $Re_\lambda = u_{rms}\lambda/\nu$ (where λ is the Taylor lengthscale), are discussed and compared in Section 3.2 as an introduction to the spectrum analysis provided in Section 3.3. For a discussion and definition of the turbulence quantities computed using the pseudo-fluid approach, please refer to Torregrosa et al. (2020) and Appendix C. The droplet statistics will be then presented in terms of size and distribution first in Section 3.4, then in terms of their relative location in Sections 3.5 and 3.6. Droplet generation over time is addressed in Section 3.7. Finally, an insight on droplet clustering using the Radial Distribution Function (RDF) is provided in Section 3.8.

3.1. Mean fields analysis using one-point statistics

A first indication on the differences between cases can be obtained by analyzing the averaged fields. Fig. 3 presents the main quantities computed with time-average operation (here, the operator $\langle\rangle$ indicates the time-average) over the time span T_{SS} on a plane Ω (see Appendix C and Torregrosa et al. (2020)). A first important consideration should be done on the values of the centerline velocity U_c and the radial position where the velocity has decayed by half of its centerline value, $r_{1/2}$. As these parameters are widely used in literature to compare jets and sprays at different injection conditions, here a special care should be devoted to their numerical value, as they are quite revealing on how the axial inlet velocity decays radially. In fact, the MBC case opens up faster than the SBC cases, therefore showing a lower axial velocity ($U_{c,MBC}/U_{c,SBC} = 0.95$) and a higher $r_{1/2}$ ($r_{1/2,MBC}/r_{1/2,SBC} = 1.16$). These ratios are also reported in Table 3, alongside the ratio in the total number of droplets N_d in the two cases. Despite both simulations are performed with the same mean velocity inlet profile, the MBC centerline axial velocity has overall decayed by a 20% (in comparison to its inlet value) while SBC roughly by a 15%.

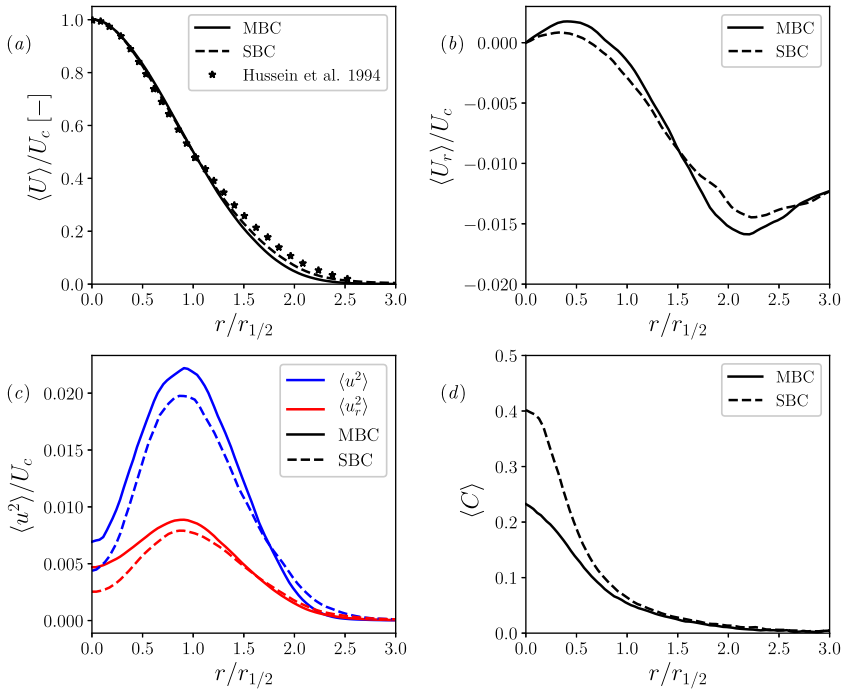

Fig. 3. Time averaged fields computed at $x/D = 25$. Panel (a) shows the radial profile for the mean axial velocity component (results are compared against experimental data from Hussein et al. (1994)). In panel (b) we show the radial profile for the mean radial velocity component. Panel (c) shows the radial profile for the velocity fluctuating components, where line colors represent the component (axial or radial) and the line style differentiate the cases. Finally, in panel (d), the radial profile for the averaged Heaviside function is shown. (For interpretation of the references to color in this figure legend, the reader is referred to the web version of this article.)

Despite the differences in the values of U_c and $r_{1/2}$, Fig. 3(a) displays a remarkable similarity in the dimensionless Gaussian distribution of the velocity for the two cases, also when compared against the results obtained in Hussein et al. (1994) for a round jet. Differences can be observed in panel (b) of the same figure, as the symmetrical profile encountered in Hussein et al. (1994) is not found, as the radial component is not yet fully developed. In a first place, it is evident that U_r positive values are significantly lower than reported in literature, where $max\left(\langle U_r \rangle / U_c\right)$ is 0.017 and it is reached at $r/r_{1/2} = 0.6$. While a similar radial position for the maximum is showed for the MBC case, the lower values of the radial velocity suggest that the spray is still in its Near-Field region in both cases. Furthermore, the tendency of air entrainment is predominant over the spray spreading (i.e. predominantly negative velocities) which is in agreement with previous hypothesis. Consistently with what has been observed in the U_c, $r_{1/2}$ discussion, the MBC case tends to have a wider radial spreading than the SBC case.

The velocity fluctuations are shown in Fig. 3(c). The maximum values for both the axial velocity fluctuations $\langle u^2 \rangle$ and radial velocity fluctuations $\langle u_r^2 \rangle$ are about 25% of values reported in literature. For $r_{1/2} < 1$ the curves slope is still strongly positive, underlining how the influence of the liquid core is still predominant in the mean flow. Again, the inconsistency against literature data supports the hypothesis that the spray self-similarity is not yet fully developed, which implies that the domain considered in the axial direction should be larger to capture self-similar flow features.

Fig. 3(d) shows the averaged color function $\langle C \rangle$ (also considerable as a volume fraction). $\langle C \rangle$ is of central importance in determining η (see Torregrosa et al. (2020)) hence for analyzing the turbulence behavior of the fluid. The MBC case presents a lower axial value of $\langle C \rangle$ which suggests a higher atomization. This assumption is consistent with the stronger radial spreading of the MBC case in respect to the SBC.

The differences between the two cases are remarkably interesting, especially considering that consistent conclusions where obtained by the authors in Salvador et al. (2018), in a parametric study of the L parameter in the SBC case. In that study, the authors highlighted how larger turbulent structures were able to increase the perturbations on the liquid surface, inducing an earlier breakup and, overall, an earlier radial spread of the spray. Despite in the present study both cases have the same L at the inlet inflow, the comparison with the results in Salvador et al. (2018) suggests that structures anisotropy in the MBC inflow generate effects similar to an increment of L. This consideration suggests that the anisotropy of the turbulent structures of the MBC case can be associated with higher turbulent kinetic energy at the largest scales of motions.

Table 3
Simulation lumped quantities ratio summary. $r_{1/2}$ in the radial position where the axial velocity U_c has decayed to $U_c/2$ and N_d is the number of droplets. The values of $r_{1/2}$, U_c and computed at $x/D = 25$.

	$r_{1/2}$	U_c	N_d
$\frac{MBC}{SBC}$	1.16	0.95	1.2

The analysis made on Fig. 3 led to the conclusion that at $x/D_n = 25$ the flow is still not self-similar. On the other hand, an important remark can be made on the usual criteria used for defining the self-similar region. In fact, it is a common approach in experimental studies to assume that the flow is self-similar when the axial velocity profile satisfies such a condition. On the other hand, this section clearly highlights how for an axial concentration of $\langle C \rangle > 0.2$ such a condition is not reached. This needs to be further addressed in future studies with larger domains, able to capture the flow transition into the fully dilute field.

3.2. Determination of the Kolmogorov scale

In this section, we present the determination and analysis of the Kolmogorov scale, using the methodology described in Appendix C and more extensively in Torregrosa et al. (2020). The importance of the Kolmogorov scale for the present study lies mainly in two reasons. In a first place, it helps to assess the quality of the simulation. In fact,

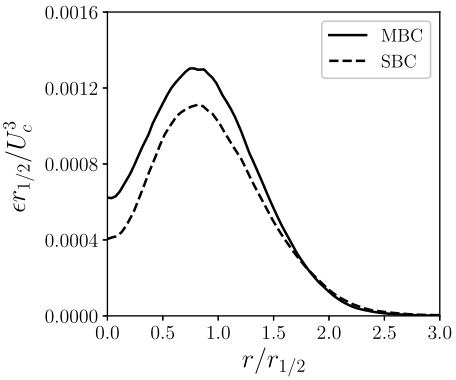

Fig. 4. Energy dissipation rate computed at $x/D = 25$.

η cannot be faithfully determined a-priori and its direct calculation requires the simulation to reach a statistically stationary state. In a second place, η provides a universal scaling factor which allows, for example, to rescale the spectrum of the two simulations in order to improve the comparability (e.g. Torregrosa et al. (2020)). Ultimately, it also allows to ensure that the difference in the types of structures forced into the system by the inflow BCs are not affecting in any way the small scales motion.

The energy dissipation rate $\epsilon = 2\langle\nu\rangle\langle s_{ij}s_{ij}\rangle$ (see Torregrosa et al. (2020)), being $s_{ij} = (\partial_i u_j + \partial_j u_i)/2$, is showed in Fig. 4. The numerical value of ϵ has been made dimensionless by multiplying it by $r_{1/2}/U_c^3$, while the value of ϵ for the SBC case is almost 1.18 times the one computed for the MBC case. The most relevant reason for that is the difference in the $\langle C\rangle$ profile in Fig. 3, panel (d), which is used to compute the average viscosity field. Aside from this consideration, the two profile are indeed showing a similar behavior and consistent with what have been presented previously.

Fig. 5 shows the radial profiles for Re_λ, panel (a), and η, panel (b). Here, η (computed as in Eq. (C.1)) is presented with its numerical value in order to improve the clarity of the comparison and to provide a numerical reference useful for comparing similar simulations in future studies. Once again, the inverse proportionality $Re_\lambda \propto 1/\langle\nu\rangle$ leads to the generation of a stronger turbulence field, hence higher values for the MBC case. On the other hand, no significant differences are observed for minimum values of η in panel (b). As it can be noted, a flat region for $r < 1.5r_{1/2}$ is found, where the value of η fluctuates between $0.5 \div 0.75$. Coherently, this region corresponds to the highest values of Re_λ observed for both simulations. Finally, we would like to remark that the current simulations do not fully resolve all scales of motion within the mixing layer, being $3 < dx/\eta < 4.5$ in this region. On the other hand, this does not affect the validity of the study, as the spectra will show no effects of this under-resolution (see Section 3.3).

The extreme similarity in the value of η deserves to be addressed. As discussed in literature, η is independent of the large scale energy and, in general, from their anisotropic or isotropic behavior (Pope, 2001). On the other hand, the analysis performed until this point are revealing significant differences in the overall spray behavior between the two simulations. Above all, the main difference is in the atomization behavior, that is clearly demonstrated by the volume fraction in Fig. 3(d). As Re_λ is indicative of scale separation in the flow, similarities in η suggest variations at large scales. Further evidences will be provided in the next section.

3.3. Spectral analysis of turbulence

The spectra of axial velocity fluctuations can be used as a tool to highlight the differences between the two cases. At a given axial and radial position, the comparison of the MBC and SBC spectra is able to reveal how the energy is distributed among scales, hence allowing quantitative comparison between the two cases.

The spectra of each physical radial position is compared for the two cases in Fig. 6. Each radial position is represented with a different color (continuous line for the MBC case and discontinuous for SBC) and its local properties are reported in the legend. It is immediately clear that in fully developed turbulent regions ($Re_\lambda > 100$) the collapse of MBC and SBC curves in the inertial and dissipative ranges is remarkably accurate. In these regions, the inertial range have a quite neat agreement with the $-5/3$ law, demonstrating that the energy transmission between scales is correctly resolved.

The most important differences in the spectrum lie in the small wavelength energy range. Here, a clear tendency is observed: the energy content of the MBC case is constantly higher than the SBC. This is a major difference between the two cases. The spectra of the two simulations present a perfect agreement at small scales and a significant difference in the energy containing range. This is the main explanation for our observations until this point. In fact, as addressed in literature by Salvador et al. (2018), Jarrahbashi and Sirignano (2014) and Zandian et al. (2018) the surface instabilities are closely connected with the nozzle turbulence, which generates radial deformations of the liquid phase that ultimately increase the shear forces and promote the breakup. The shear stress generates a number of hairpin turbulent structures that promote the formation and detachment of liquid structures (Jarrahbashi et al., 2016). Furthermore, larger eddies are responsible for the differences in such a process as they are the ones with a sufficient energy level to disrupt or perturb the liquid surface of large and continuous regions of liquid. Therefore, results suggest that the anisotropic structures of the MBC case favor the liquid breakup and the formation of more energetic eddies. It is likely that the relation between eddy size and liquid breakup could be inferred in future studies.

3.3.1. General remarks on spray spectra

From a multiphase flow prospective, it is important to contextualize the spectra displayed in Fig. 6. In cases with solid particles analyzed as Lagrangian particles ($d_v > \eta$) or point particle ($d_v < \eta$) a deviation at higher wavenumbers is observed due to the absorption of part of the kinetic energy by the particle motions (Sundaram and Collins, 1999; Burton and Eaton, 2005). Related works from Lucci et al. (2010) analyze two way coupling in particle laden flows with decaying turbulence, observing spectra deviation due to the disruption of larger-eddies from particles. In Homogeneous Isotropic Turbulence (HIT), works by Dodd and Ferrante (2016) and Duret et al. (2012) have highlighted how surface tension forces are likely to generate energy increments at higher frequencies. Spectra deviations were also experimentally found for bubbly flows (Prakash et al., 2016). On the other hand, in atomizing flows (e.g. Ling et al. (2019), Torregrosa et al. (2020) and Pitsch and Desjardins (2010)) no deviations of spectrum from the $-5/3$ is observed, nor energy injection at any scales. As this behavior is partially in contradiction with the results obtained on other multiphase flows, it requires to be carefully addressed. In a first place, let us depict a qualitative picture of the droplets movement in the flow. Intuitively, liquid structures generated by the intact core breakup have two main advection directions. On one hand they can be advected axially by drag generated from the high axial momentum. Alternatively, droplets can be transported radially towards less turbulent regions. As the spectra displayed in Fig. 6, are taken in the subdomain Ω (which is at a fixed axial position) the axial droplets transport mechanism is less observable. Therefore, as a droplet progress radially, it encounters a progressively less dens media, where coalescence is therefore reduced. Furthermore, also breakup is likely reduced, given the decreasing turbulence intensity. The reduction of these two mechanisms, compared to works such as (Dodd and Ferrante, 2016), generates a significantly different scenario, which may explain the lack of spectra deviations. Another interesting comparison can be performed against

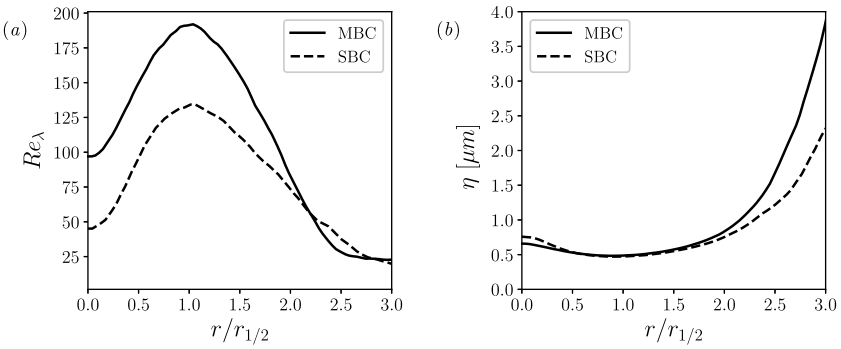

Fig. 5. Time averaged radial profiles for Re_λ, panel (a), and Kolmogorov scale, panel (b). All quantities are computed at $x/D = 25$.

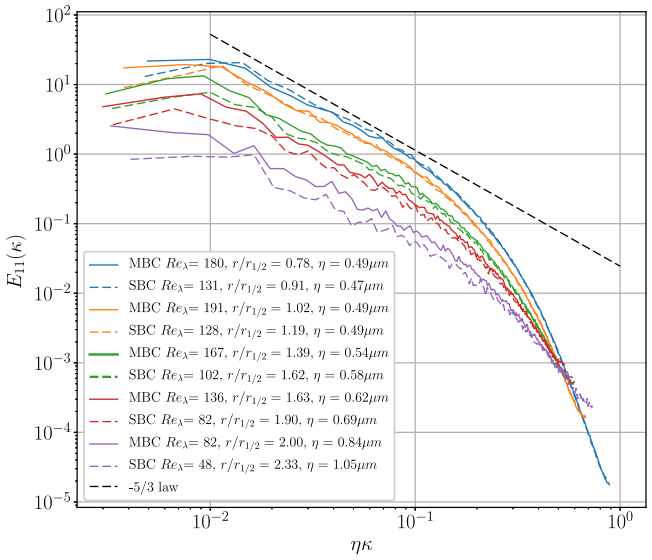

Fig. 6. Spectra of the axial velocity autocorrelation, performed over the azimuthal coordinate. In the legend, each series presents information on the radial position as a function of the $r_{1/2}$, as well as the local value of Re_λ and η for reference with previous figures. All the energy spectra are computed at $x/D = 25$.

data from Rosti et al. (2020), where the spectra modifications are less and less prominent as the initial size of the droplets increases. Here, the "larger droplet" size, should be considered as the nozzle diameter, hence located at very low frequencies in the spectra. By contextualizing the findings in Rosti et al. (2020) to the present study, it can be observed that this is actually in agreement with the idea that in strongly anisotropic flows, as the characteristic size of the larger liquid structure increases, the spectra modifications occur at progressively higher frequencies and in less prominent ways. These discussion opens the way to two considerations: the first one, although trivial, is that there is no concrete and definitive tool and interpretation on how to analyze turbulence in multiphase flows. The second one is that more information on sprays can be achieved by an accurate analysis of the droplet topological behavior, which will be addressed later in the paper (Sections 3.4, 3.5 and 3.8).

3.4. Droplet size and properties distribution

A deeper understanding of the simulation results can be provided by analyzing how the droplets are distributed. A droplet description can be reduced to its position $\mathbf{x_d}$, its velocity $\mathbf{u_d}$ and its diameter d_v. This determines, in the most applicable scenario, a 7-dimensional space for the droplet description. In literature of point-process systems, such a representation is classified as a Klimontovich description of the system (see Subramaniam (2000) for its application to sprays). While for many fluids some of this dimensions can easily be lumped or neglected (e.g. $\mathbf{x_d}$ in particle laden isotropic turbulence boxes (Park et al., 2017)) sprays displays, at least, 2 main direction of development, the axial and the radial. Furthermore, a description of the atomization patterns can be provided by understanding which is the typical droplet size distribution and how much of the kinetic energy of the liquid core is retained by atomized droplets. In the following sections, a droplet is defined as a continuous region of liquid, regardless of its shape or size. Further details on their detection algorithm and related observations can be found in Appendix B.

Fig. 7 shows the probability of droplet size distribution expressed as $\mathcal{P}_{d_v} = N/N_{tot}$ where N_{tot} is the total number of droplets. In a first place, it must be noted that the MBC case displays more atomization than the SBC case, given that $N_{tot,MBC}/N_{tot,SBC} = 1.2$. This should not be discredited as marginal, as such an increment in atomization means a significantly higher mass loss in the spray core. In this case, it is evident that the turbulent isotropic structures induced by the SBC case are less prone to trigger atomization than the anisotropic structures produced in MBC.

Aside from the total droplet count, Fig. 7 highlights an interesting aspect of the atomization phenomena. In fact, the probability function $\mathcal{P}_{d_v}$ is remarkably similar for the two cases suggesting that, despite total number of droplet differs significantly, the way in which the ligaments form and the spray breakup occurs follows a similar pattern. This similarity helps to assess the quality of the droplet analysis (as all the mass lost has to convert into droplets). As already addressed in Section 3.3 the only significant difference in the one-dimension kinetic energy spectrum can be located at the largest scales. In this context, this could reinforce the conclusion that the larger turbulent structures are responsible for the detachment of large liquid structures from the liquid core. Once the larger liquid structures are detached from the liquid spray core, smaller eddies act as surface perturbations that prompt atomization and further breakup. This hypothesis, although difficult to definitively prove with this simulations datasets, would be in agreement with the Kolmogorov hypothesis of log-normal distributions resulting from fragmentations and its consequent fractal behavior, observed in liquid sprays by Marmottant (2001) and Chehroudi and Talley (2004) and elegantly summarized in Gorokhovski and Herrmann (2008). On the other hand, its proof would rely on droplet tracking and breakup detection, which is very computational demanding and difficult to perform, especially in conjunction with the extraction of the turbulence statistics reported above. Furthermore, it is likely that some type of two-way coupling between surface instabilities and turbulence could be identified in future studies, dedicated to analyzing coalescence and breakup in sprays.

As a droplet detach from the liquid core, two scenarios are possible from a kinematic standpoint, already briefly introduced when interpreting the spectral results. Either the droplet is advected by the main flow or is deviated towards the spray periphery. Being this study carried over in the NF region, where high average density can still be

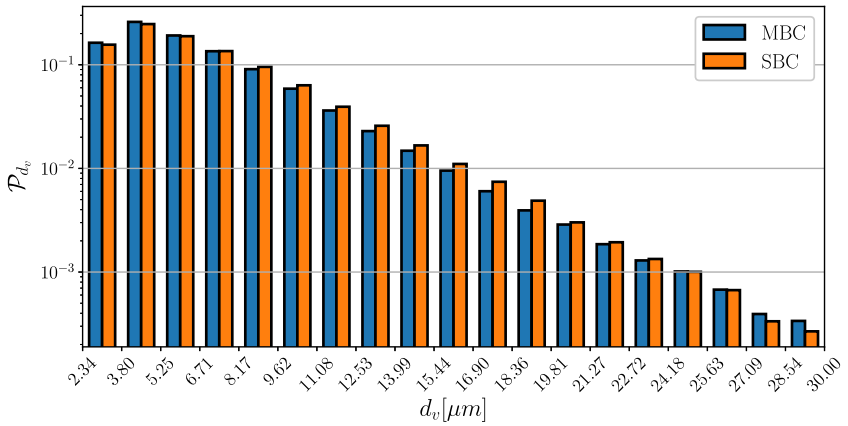

Fig. 7. Probability of droplet size distribution.

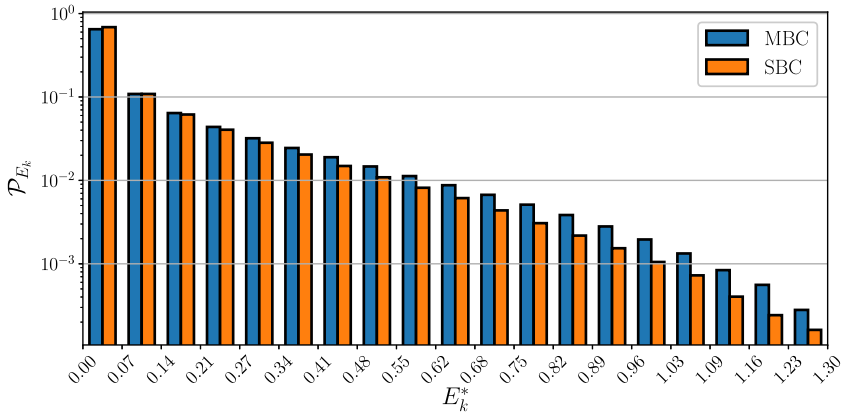

Fig. 8. Probability of droplet kinetic energy distribution. The kinetic energy is made dimensionless by dividing by the injection kinetic energy $E_{inj} = 1/2\langle U\rangle^2$.

found on the spray axis, the first scenario is quite likely to occur for droplets that have just detached from the liquid core and that have not yet reached a significant radial penetration. Furthermore, as the radial velocity component is still significantly smaller than the axial and considering a rapid decaying Gaussian axial velocity profile, a droplet will rapidly lose velocity the further it gets from the spray axis. These considerations suggest that the droplet kinetic energy E_k is a good indicator to have an understanding of the behavior of droplets in the 3 dimensions $\mathbf{u}_d$ by lumping them via a physical parameter.

Fig. 8 shows the probability function for the droplet kinetic energy. In this Figure, the kinetic energy of each droplet is made dimensionless by dividing it for the injection kinetic energy $E_{inj} = 1/2\langle U\rangle^2$, giving $E_k^* = E_k/E_{inj}$. The expectancy of $\mathcal{P}_{E_k}$ at low kinetic energy values is significantly higher than other values, suggesting that many droplets have reached a quasi-rest state, hence a significant distance from the spray axis. Discussions available in literature (Shinjo and Umemura, 2011; Salvador et al., 2018) suggest that these droplets are generated by the bending of the spray front into the typical mushroom-like shape. The peripheral liquid sheet is then teared by aerodynamic shear given by the large toroid-eddy generated on the front. This eddy usually displays $|\mathbf{u}| \approx 1.5\langle U\rangle$ tangential to the toroid and in the opposite direction of the main flow (Shinjo and Umemura, 2011; Salvador et al., 2018). Once this transient phenomenon is passed, the velocity of the droplets generated by the spray front rapidly decay due to the aerodynamic drag provided by the spray core. These droplets are likely the ones that display a very small E_k in Fig. 8.

To have a better insight on how the kinetic energy is distributed among droplets, Fig. 9 shows the joint PDF for the dimensionless kinetic energy E_k^* and the droplet diameter d_v. In order to improve the data readability, the contour coloring is logarithmic and the values are divided by the maximum value, hence no color scale is reported. Fig. 9 shows that, despite droplets of any diameter have the possibility of having very low kinetic energy, most of them are among the ones with the smaller diameter. Once again, the MBC case and the SBC case show a consistency in the described patterns. Finally, the resulting PDF from Figs. 7 and 8 is showed in Fig. 10 where a log-normal like distribution is shown for the PDF of the droplet diameter PDF, panel (*a*), and an exponential decay for the kinetic energy, panel (*b*).

The existence of droplets with kinetic energy higher than the injection kinetic energy (in Fig. 8) also needs to be discussed. Although this may seem physically unrealistic it should be noted that the mean velocity U_b at the spray inlet differs from the centerline velocity due to the characteristic velocity profile of the wall-bounded flows. This result in $U_c/U_b = 1.35$. Obviously, these droplets are expected to be along the centerline.

Aside from the singularities in the extreme regions of the flow explained above, Fig. 8 shows an exponential decay of the number of droplets with increasing kinetic energy.

3.5. Droplet radial position

The mere description of the radial position of each droplet (which examples can be found in Salvador et al. (2018)) may be interesting for general spray characterization, but is insufficient for a statistical description of the spray. In fact, round sprays are conical in nature at sufficiently high Reynolds numbers and their spray angle changes with the considered axial position, as described in Benajes et al. (2017). In particular, the spray cone angle changes significantly depending on whether the dense region or the dilute region are considered. In the first case, it is difficult to define a spray cone angle as in experimental

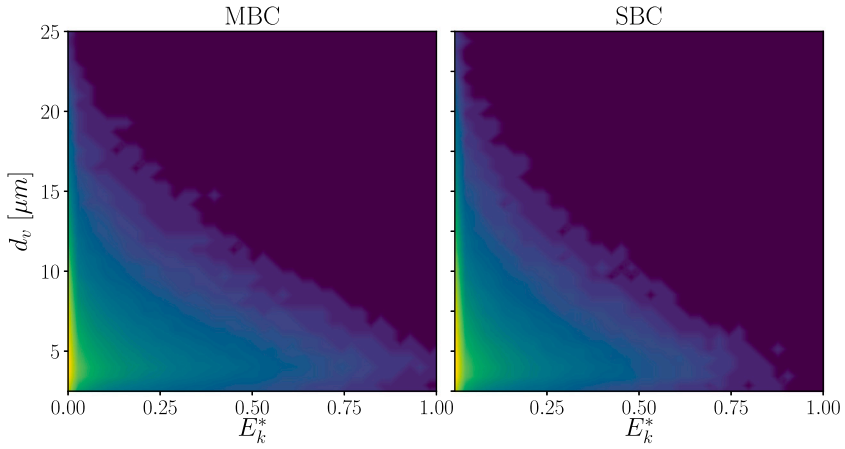

Fig. 9. Joint PDF of droplet diameter d_v and dimensionless kinetic energy E_k^*.

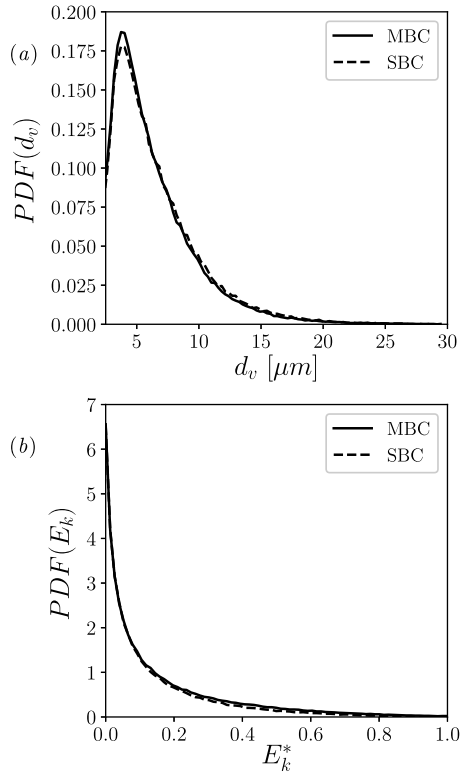

Fig. 10. Time averaged PDF of droplet diameter, panel (*a*), and normalized kinetic energy, panel (*b*).

visualization. When the spray enters the dilute region, it is easier to define a set of straight lines defining the spray cone projection over the image plane. For this reason, the droplets radial distribution is showed in conjunction with the corresponding axial position which gives a complete understanding of the space occupied in the pseudo-cone described by the spray.

Fig. 11 shows the joint PDF for the radial position (divided by its axial position) and the axial position (divided over the total x-length l_x). As done before, the contour is logarithmic and normalized by its larger value. This figure shows that for $0 < x/l_x < 0.5$ in both cases no angle is yet formed. This region shows a number of droplets which are pushed quite far from the spray axis. The analysis of the time sequence of the snapshots reveals that these droplets are not generated in the spray when the statistical stationary state is reached. In fact, these droplets are generated by the spray tip during its transient penetrations and, for reasons explained previously, they rapidly lose kinetic energy until they reach a negligible velocity in comparison with the spray injection velocity. As a matter of fact, similar values for the tip radius during the transients are found in Shinjo and Umemura (2011). For $x/l_x > 0.5$ a pattern is observed, as droplet clusterize in $r/x < 0.15$. Here, droplets probability $\mathcal{P}$ reaches an asymptotic behavior, which indicates the formation of a cone angle. This behavior is expected to be maintained in the dispersed region.

In general, Fig. 11 shows a distinct pattern for both cases and it reinforces, once again, the idea that no significant differences in the atomization patterns can be observed from the droplet topological analysis. It is also interesting to notice that the larger turbulent scales have no significant effect on the general droplet spread behavior, while they affect the total number of droplets generated.

3.6. Spray axial development

Fig. 11 already gave a first grasp of how the droplet are distributed axially, but still the total number of droplets at each radial position should be addressed.

Fig. 12 shows the probability $\mathcal{P}(x)$ of finding droplets at a given axial position (normalized by the nozzle diameter D_n); below the curve, two time-averaged contour of the volume fraction in the simulation are showed respectively from the MBC and the SBC cases. After a non-atomized region (for $x/D_n < 2$) both cases start atomizing and, after a steep region at $2 < x/D_n < 5$, the probability $\mathcal{P}(x)$ for the two cases collapse again, into an extremely similar behavior. Despite this similarity, the axial time-average of the volume fraction decays significantly faster in the MBC case. This behavior is in agreement with the higher number of droplets generated from the MBC case. In the steeper region of $\mathcal{P}(x)$, for $2 < x/D_n < 5$, a certain correspondence can be found between the start of such a region and the axial shrinking of the liquid region, although the liquid region does not end when the steeper region stops. This is in contrast with what deduced in experimental analysis (e.g. Benajes et al. (2017)), where the conclusions drawn from the external optical characterization of the spray suggested the end of the intact core length to coincide with the end of the steeper region of $\mathcal{P}(x)$.

The comparison of the volume fraction also supports the idea previously stated, that the low frequency turbulent structures are responsible for the large liquid structures detachment. Furthermore, it is interesting to understand how the droplet size is distributed at each axial distance. In fact, this would help understand what are the drivers which generate atomization at each axial position.

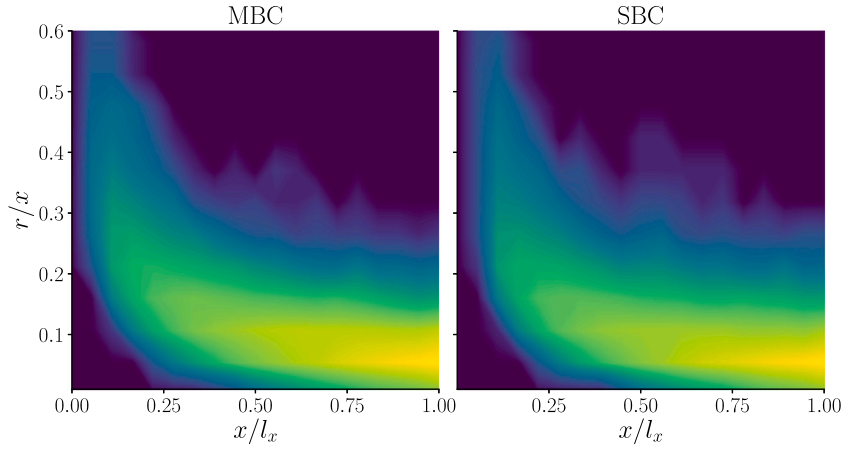

Fig. 11. Joint PDF for the droplet radial position r (normalized by its axial position x) and axial position x (normalized by its axial total length l_x).

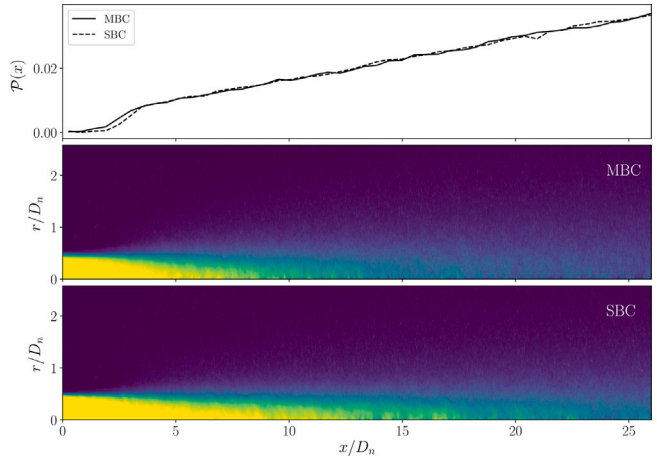

Fig. 12. Probability $\mathcal{P}(x)$ of droplet presence as a function of axial position (top). Below, simulation time-averaged contours of the volume fraction as a function of the radial position as well as the axial distance, both normalized by the nozzle diameter D_n. The x-axes of the figures are aligned.

Fig. 13 shows the probability function $\mathcal{P}(d_v)$ at various axial position from $x/D_n = 2.5$ to $x/D_n = 25$ at increasing gray-scales. The number of bins for the droplet diameter has been reduced to increase the curve resolution as less droplets were available at each axial position (especially at lower values of x/D_n). As previously described, it is interesting to notice that at early axial positions most of the droplets generated are of small size where larger d_v are almost nonexistent. Again, this is because, as previously assessed, most of the droplets in this region are just created by the spray tip, which is an isolated phenomenon in the simulation transient. While increasing the axial position, the curves converge over a more evenly distributed diameter size and towards a distribution similar to what has been obtained in Fig. 7. Again both curves converge towards the same distributions although, for low penetrations, the MBC case is more biased towards the generation of smaller droplets.

3.7. Generation of droplets over time

Time characterization of droplets generation can be used to determine differences between the two cases and information on the spray behavior. While many approaches could be used for this purpose, we chose to be consistent with the methodology used in Sections 3.4 and 3.6 and show, in a first place, the temporal generation of droplets grouped by size.

Fig. 14 shows the generation of droplet within a size range (reported in the legend) in terms of total mass per diameter range M_d. The sets of curves have been divided over two figures to improve readability and only ranges with significant mass are showed. The spray tip reaches the end of the domain at $t_{end} \approx 27$ µs while the statistics showed in Sections 3.4 and 3.6 are taken for $40\ \mu s < t < 300\ \mu s$. Until t_{end}, all droplets sets display a linear increment of mass, which is extremely neat for those sets where a high droplet number is available for statistics (e.g. $d_v < 10\,\mu m$). The correspondent time-averaged slope, expressed as dM/dt (for $t < 30\ \mu s$) is showed in Fig. 15(*a*). As obvious for this part of the simulation, all the derivatives are positive, and a clear trend can be observed.

It is immediately evident that droplet sets that are of high relevance in droplet diameter distributions statistics, such as $d_v < 5.5\,\mu m$ are less relevant from a total mass standpoint. In fact, it can be observed how significant importance is gained by droplets for which $5.5\ \mu m < d_v < 12.5\ \mu m$. As there are no evidences that a sufficient mesh size has ever been achieved for fully turbulent atomizing sprays, this trend suggests that non-fully-resolved DNS simulations (at least from an atomization standpoint) may still be useful tools for providing data for sub-grid models and for improving the understanding of the spray behavior.

After the total spray penetration has been reached, still a quite clear trend can be observed as the simulation reaches a statistical stationary state. In order to do so, similarly to what was previously discussed for the transient, Fig. 15(*b*) shows mass generation over time for the different droplet size. As widely discussed before, we hypothesized that the smallest droplets are generated by the spray tip, therefore it is likely to see that their generation rate decrease as shown for $d_v < 10\ \mu m$. Globally the total number of small droplets decrease in the statistically stationary state. In fact, it is likely that aside from a reduction in their production, overall a significant amount of coalescence is occurring, justifying a negative value of the derivative. On the other hand, there is still a slight production of droplets for $d_v > 10\ \mu m$ but significantly smaller than what achieved during the initial transient. A zero-mean value for dM_d/dt is likely not possible to be reached. As droplets detach from the spray core in the statistical-stationary phase of the injection, they can either be transported outside the domain (i.e. by the main flow) or they can be pushed towards the periphery of the spray and lose all their momentum. In this second scenario, droplets will not be able to exit the computational domain, as their position is too far from gas regions with high-momentum and their advection is not possible. Therefore they can either accumulate (i.e. contributing to increase

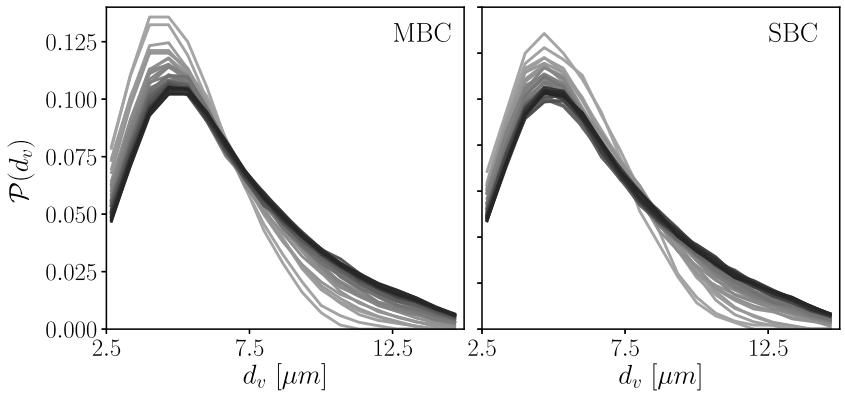

Fig. 13. Probability $\mathcal{P}(d_v)$ for droplet size. The lines goes from gray to black for $x \to l_x$. The axial distance goes from $x/D_n = 2.5$ to $x/D_n = 25$.

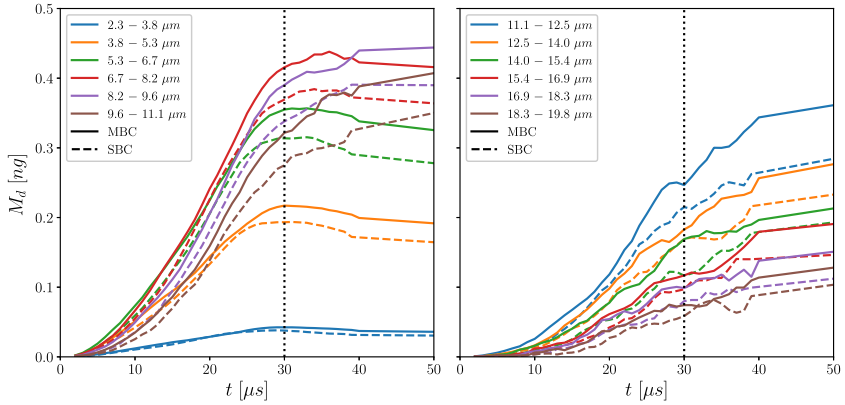

Fig. 14. Total droplet mass divided by droplet size range, displayed as a function of time. The 2 plots represent the same study at different ranges and have been divided for clarity.

the value of dM_d/dt for the specific droplets size-range) or possibly merge with other droplets that are transported in the nearby regions. Therefore, the statistical stationary state for droplets generation is described by a convergent value of dM_d/dt.

It is clear that most droplets are generated in the transient phase of the spray before a complete penetration occurs. To show this behavior, Fig. 16 the ratio between the total mass of droplets M_d and the total injected mass M_{inj} over time. Before t_{end} the total amount of injected mass grows faster than the total mass injected. Overall, the MBC accounts for more atomized mass, although the ratio is less prominent than what discussed previously for the SBC case, showing that most of the droplets generating the discrepancy are of small size (hence less appreciable in mass terms). At $t > t_{end}$, M_d increases way slower than the total amount of mass injected M_{inj} (which keeps growing linearly with time), hence the curves collapse towards a hyperbole.

Indeed, this consideration highlights the fact that most of the droplets are generated by the transient phase. The aerodynamic shear, which is the main driver generating the turbulence necessary for triggering atomization is responsible just for a small amount of the droplet generated hence it is likely that the effects generated by the anisotropic structures of the MBC are far more important in the initial transient, although no easy explanation can be provided with the data available in this study.

3.8. Radial distribution function analysis

One of the advantages of treating a spray as a point-process is that the droplet statistical location can be resumed by very few parameters in the disperse region. One of them, and maybe the most important, is the relative distance between droplets, namely the RDF.

As already mentioned in Section 3.4, the droplet discretization used here has the inherited possibility of treating the spray by means of a Klimontovich approach (Subramaniam, 2000). In this case, if the temporal evolution of the spray is neglected, the fine-grained statistical discrete function that describes the spray depends only on velocity **u**, location **x** and diameter d_v. All three variables have been statistically characterized above, but no information has been provided on distance between droplets. In statistical mechanics, as well as in point-process, this information can be summarized into the RDF. Intuitively, this function characterizes the probability of finding a droplet at a specific distance from another one, given that all droplet positions are known and that each distance between a droplet pair is computed at their mass center. This probability can then be compared to the case in which all the given droplets are equally distributed along the domain. A simple mathematical description of this function can be given by:

$$RDF(r_i) = \frac{N_{p,i}}{N_p} \frac{V}{\delta V_i}. \tag{6}$$

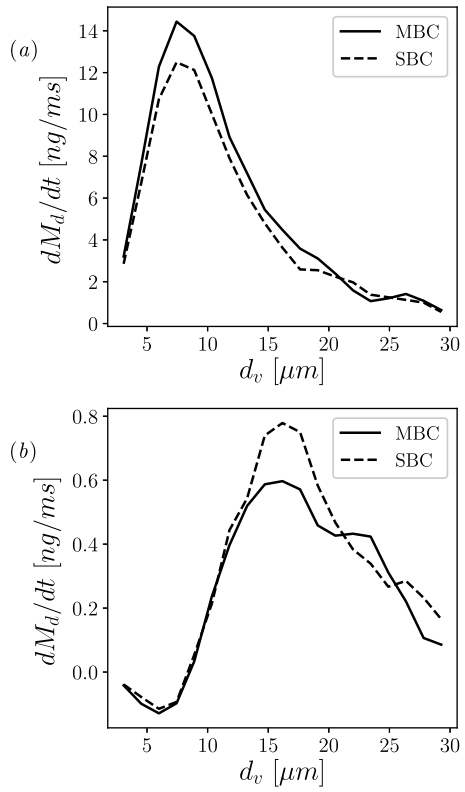

Fig. 15. Averaged droplets generation rate as a function of the droplet diameter for the transient phase, panel (*a*), and the statistically stationary phase, panel (*b*).

where $N_{p,i}$ is the total number of droplets pair at a distance contained in a sphere shell of radius r_i and volume δV_i divided by the uniform droplet pair distribution N_p/V where N_p is the total number of droplet pair and V is the total domain volume.

It is worth notice that the definition in Eq. (6) is useful in experiments and in particle laden simulation, where the droplet uniform distribution has an actual sense, given the geometry of the physical problem. It is the authors opinion that for sprays this definition should be revisited in future studies. The geometry of sprays, as already widely discussed, can be well characterized by a cone where the angle can be defined by the radial mass concentration (see Benajes et al. (2017)). In a domain as the one used here, there will be a significant portion of the domain that will not be populated by droplets and that will offset the RDF function. On the other hand, the values obtained here are comparable with data found in literature (Sahu et al., 2016; Park et al., 2017), hence likely capturing the clustering of smaller droplets. As the discussion of this topic could be complex in the dense region, this problem is destined to future works.

Fig. 17 shows the RDF for the MBC (left) and the SBC (right) cases. As the number of smaller droplets ($d_v < 15$ µm) is significantly high, smoother statistics are obtained, while for larger droplets a noisier signal is found. Very small droplets have the tendency to cluster together. As the droplet size increases their clustering decrease and a minimum is found for $d_v \approx 10\,\mu$m. Finally, as the diameter increase further, droplets again tend to form clusters. These trends are likely due to different phenomena. Smaller droplets are easier to advect due to their low mass, therefore tends to follow the small-particle behavior, hence forming clusters in low turbulence regions. Larger droplets are mostly formed in the spray core and have a significant inertia, as well as total mass. While these factors would lead to the conclusion that these droplets should disperse, the fact that most of the velocity in the spray core is still predominantly axial, cause these droplets to still penetrate axially, therefore their dispersion is relatively low.

4. Conclusions

In the present work, the analysis of two different cases, namely SBC and MBC, allowed to understand and quantify the influence of turbulent structures shapes, in principle described by the same integral quantities L and I, on the spray breakup and atomization. The effects of these structures is quantified both from analyzing the resulting turbulent field generated in the NF and by analyzing in depth droplet statistics. The discussion performed in Sections 3.2 and 3.3 is particularly revealing. Here, data show that an a-priori determination of η for this kind of multiphase flows is likely to be fairly inaccurate. This simple correlations in fact neglect the complexity of the flow in the mixing area of the dense region. The spectra demonstrates that the unresolved energy is a negligible percentage of the total one, hence the information loss does not prevent to obtain significant results. On the other hand the smallest scale for atomization DNS is still to be reached and, as discussed in literature (Pitsch and Desjardins, 2010), will likely require the development of more suitable numerical techniques able to resolve up to the phase-interface thickness.

Despite these limitations in modern multiphase DNS simulations, some interesting contribution about the flow spectra have been achieved. In a first place, the pseudo-fluid method for obtaining spectra was used to achieve smooth spectrum and to understand how the energy distributes among scales at different radial positions of the spray. The same tool was used to quantify the differences in the Fourier coefficients at large scales, providing an explanation on the different breakup dynamics occurring in the two cases. The differences in the one-point statistics allow to assess that the current domain is still far from reaching the full axial self-similarity described in literature for jets and sprays in the disperse region. Despite that, this work contributes in the understanding of the transition from near-field to far-field and how the velocity profiles behave when affected by different nozzles (here represented by the differences in the turbulent structure shapes). We believe that, in order to confirm the self-similar properties of sprays in the dispersed region, future simulations will have to aim at larger domains.

The droplet analysis allows to improve the understanding on how turbulence affects breakup. In fact, the small differences in probability (and probability density) functions highlights how Re and We, here constant for both the MBC and the SBC cases, are still the main parameters that need to be investigated in these flows in order to capture differences in the atomization behavior. While anisotropic structures trigger a significantly stronger atomization, the overall probabilities are not significantly different, showing that nozzle turbulence could be used to accelerate the spray breakup but not to control the atomization behavior if the same turbulence parameters are maintained.

A study of the spray topology reveals consistent patterns. For both cases, the probabilities for droplet axial and radial positions have been analyzed, revealing how, despite the significant differences in the total number of droplets generated, the patterns of atomization for the two cases are quite similar. Similar conclusions are also drawn from the droplet time generation and their generation rates.

Overall, some interesting considerations can be drawn. In a first place, it is important to observe that the different total number of droplets generated and the differences in the one and two point statistics (analyzed in dimensional space) seem to point towards the conclusion that for engineering purposes, the inlet boundary conditions are of fundamental importance in determining the atomization behavior of a spray, especially in light of its applications in combustion studies.

On the other hand, all the analysis performed reveal similar patterns, showing how the overall atomization physics is dictated mainly by Re and We of the studied cases. While this conclusion seems

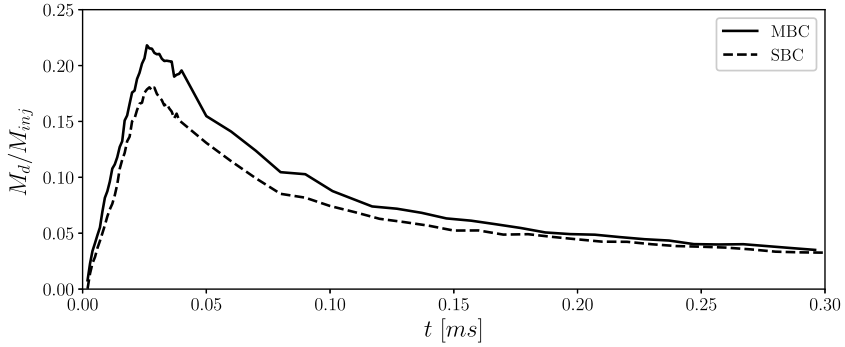

Fig. 16. Total mass of atomized droplets over the total mass injected as a function of time.

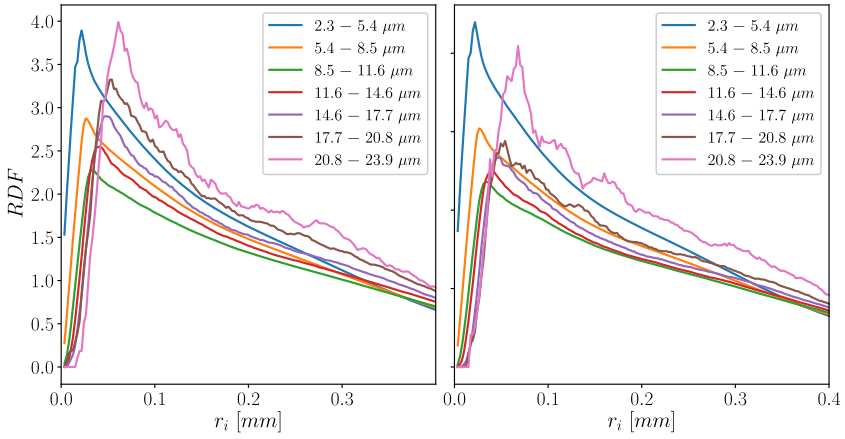

Fig. 17. RDF for droplets' ranges (reported in legend). On the left, the MBC case is showed while the SBC case is showed on the right.

trivial, it may actually have profound implications. As turbulence and atomization are usually topics addressed as chaotic processes, the usage of different initial and boundary conditions could dictate severe differences in their development. Such differences are not observed here. In other terms, this opens for future research on the fundamental dynamics generating this phenomena in a possibly deterministic way.

CRediT authorship contribution statement

Marco Crialesi-Esposito: Investigation, Formal analysis, Methodology, Writing – original draft. **L.A. Gonzalez-Montero:** Formal analysis, Software. **F.J. Salvador:** Supervision, Conceptualization, Writing – original draft.

Declaration of competing interest

The authors declare that they have no known competing financial interests or personal relationships that could have appeared to influence the work reported in this paper.

Acknowledgments

This research has been partially funded by Spanish Ministerio de Economía y Competitividad through project RTI2018-099706-B-100, "Estudio de la atomizacion primaria mediante simulaciones DNS y técnicas ópticas de muy alta resolucion". Additionally, the authors thankfully acknowledge the computer resources at MareNostrum 4 (Barcelona Supercomputing Center) and their technical support provided by FI-2017-2-0035 and TITAN (Oak Ridge Leadership Computing Facility) in the frame of the project TUR124.

The authors would like to thank Dr. S. Zaleski for the useful conversations that lead to the droplet topological analysis. We would also like to thank Dr. S. Hoyas for his help and advice in studying the turbulent nature of the flow.

Appendix A. LES methodology and validation

The LES simulation was performed using the open-source code *OpenFOAM*. The geometry used is a cylinder with diameter equal to D_n, reported in Table 1. The cylinder length have been defined according to literature data, as the ratio l_n/D_n (with l_n being the nozzle length) have significant effects on the correct development of turbulent structures (Eggels et al., 2006). El Khoury et al. (2013) used a $l_n/D_n = 12.5$ for a Re_b of 5300, quite similar to the one simulated here (see Table 1), concluding that the findings on (Wu and Moin, 2008) $l_n/D_n = 7.5$ had a sufficient length for the axial structures to propagate. Consequently, we set $l_n/D_n = 8$ based on these considerations. In order to successfully initialize turbulent structures in the LES domain, we imposed an isotropic turbulence field thanks to the spectral methods proposed by Rogallo (1981).

The solver *pisoFOAM* is used, based on the PISO algorithm (Issa, 1986), to solve the following governing equations:

$$\frac{\partial \widetilde{u_i}}{\partial t} + \frac{\partial \widetilde{u_i u_j}}{\partial x_j} = -\frac{1}{\rho_l}\frac{\partial \widetilde{p}}{\partial x_i} + \nu \frac{\partial}{\partial x_j}\left(\frac{\partial \widetilde{u_i}}{\partial x_j} + \frac{\partial \widetilde{u_j}}{\partial x_i}\right) \tag{A.1a}$$

$$\frac{\partial \widetilde{u_i}}{\partial \widetilde{x_i}} = 0 \tag{A.1b}$$

where $\widetilde{u_i}$ is the filtered velocity field, ρ_l is the liquid density (constant, as reported in Table 1) and $\widetilde{p}$ is the filtered pressure field. The subgrid scale model chosen is the *Wall-Adaptive Local Eddy-viscosity* where the term $\widetilde{u_i u_j}$ in (A.1a) is rewritten as:

$$\widetilde{u_i u_j} = \tau_{ij} + \widetilde{u_i}\widetilde{u_j}. \tag{A.2}$$

Here, τ_{ij} is the residual (or subgrid) stress tensor, which is modeled according to Nicoud and Ducros (1999).

Finally, the simulation is performed at a fixed time-step of 20 ns for a time equal to $N_w = 60$ in order to allow for reliable statistics.

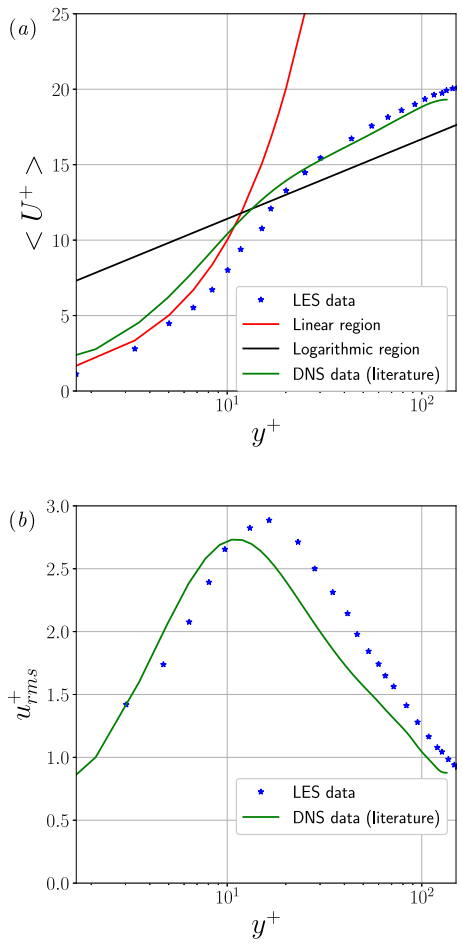

Fig. A.18. Validation of the LES simulation against literature DNS data provided by Eggels et al. (2006). Panel (*a*) shows the wall-law, plotted using the dimensionless mean velocity while the root mean squared velocity is shown in panel (*b*).

A.1. Validation and analysis

In order to validate the simulation outcome, the results have been compared to literature data from Eggels et al. (2006) for both, the average velocity and the root mean squared components in Fig. A.18. Both plots are showed as a function of the dimensionless wall distance $y^+ = yu_\tau/\nu$, where y is the distance from the wall and u_τ is the shear velocity. Fig. A.18(*a*) shows the LES simulation validation for the dimensionless mean velocity $\langle U^+ \rangle = \langle \tilde{u} \rangle / u_\tau$. In this figure, a good agreement between the LES data and the DNS data (from Eggels et al. (2006)) is demonstrated. Panel (*b*) of the same figure shows the dimensionless root mean squared velocity $u^+_{rms} = u_{rms}/u_\tau$ where, although the general behavior is well captured, the results are clearly showing a displacement in the direction of higher y^+. This error in Fig. A.18 leads to the discussion about the mesh size difference between the LES and the DNS simulation and why, this error, is overall negligible. The necessity to resolve the wall-induced shear, implies a mesh refinement in the wall region of the LES simulation, while the DNS, using a Cartesian grid, has a constant mesh size (see Table 2). While an interpolation will be mandatory in order to adapt the solution to the coarser DNS mesh, this will also imply that some frequencies will be filtered out. Furthermore, a case can be made that surface tension inherently dumps the effect of smaller eddies (Milgram, 1998), largely developed in the near-wall region. While it remains to be proven that small wall structures are not a major influence on the atomization process (especially in the generation of smaller droplets), the needs for an interpolation simplifies the comparison between MBC and SBC. In fact, this filtering procedure will force the smallest eddies to be removed by the LES solution, hence enhancing the comparability between the MBC and the SBC cases. More specifically, the SBC case uses a synthetic turbulence algorithm which will generate turbulent structures as large as the turbulent integral lengthscale L and as small as the mesh size dx. This method is based on two main steps (which are better explained in Salvador et al. (2018) and Klein et al. (2003)): at first, the hypothesis of homogeneous turbulence (and the consequent autocorrelation function proposed by Davies and Batchelor (2007)) is used to filter a matrix of random numbers in order to generate a randomly coherent smooth field. Afterwards, the resulting field is adapted to the specific case by using the profiles showed in Fig. A.18, the turbulence intensity I and the turbulent length-scale L. The derivation of the latest two parameters from an LES simulation will be discussed later on in this section.

While for smaller scales the hypothesis of homogeneous turbulence may be acceptable (as an extension of the local isotropy hypothesis formulated by Kolmogorov), it is most likely not the case for larger scales of motion, close to the integral length scale. Fig. A.19 displays the turbulent structures detected using the Q-criterion algorithm by Jeong et al. (1995) colored by the local vorticity. This snapshot (performed after 30 washouts) shows a major axial orientation of the turbulent structures, which are advected by the main flow, suggesting an anisotropic action of the velocity components. While an in-depth discussion of anisotropy in wall-bounded flows across the scales is outside from the scope of this paper, a full discussion on the topic can be found in the work of Biferale and Procaccia (2005).

A.1.1. Velocity interpolation from LES to DNS simulation

Once the LES results have been validated, the data can be interpolated into a Cartesian mesh for usage in ParisSimulator. As previously observed, the larger structures can be faithfully reproduced thanks to the l/D_n. On the other hand, accurately reproducing the behavior of smaller structures close to the wall is particularly challenging. The main reason is that the wall spacing in the LES simulation is $dx_{LES} \approx dx_{DNS}/30$ (and increase exponentially), thus significantly smaller than the DNS mesh. This mesh size corresponds to a $y^+ = 0.3$, more than sufficient for an accurate solution of the wall. For this discrepancy in mesh size, it is important to notice that the wall behavior, as well as the smallest turbulent structures of the LES, will not be accounted for in the DNS. In order to reproduce the mean flow (see Fig. A.18(*a*)) it is not significant, as a linear region can easily be reproduced with only two points. On the other hand, the velocity fluctuations, especially at their peak (panel (*b*)) will be attenuated to only 4 grid points (see Fig. A.20).

As previously mentioned, while this simplification may represent an incomplete representation of the LES results, it improves once again the comparability between the MBC and SBC simulations, where the effect of the most turbulent region is under-resolved. Furthermore, a case can be made (Milgram, 1998) that surface tension inherently dumps the effect of smaller eddies, largely developed in the near-wall region. Furthermore, a Cartesian mesh resolved up to δ_{LES} is unfeasible even for state of art DNS simulations (Ling et al., 2019; Hasslberger et al., 2019).

Finally, this effect, while worth mentioning, is considered to be irrelevant for the present study.

Appendix B. Droplet detection algorithm

Droplet detection (sometime referred to as tagging) has been widely used in multiphase flows in general for bubbles and droplets. The application of this methodology to Lagrangian Point-Particle (LPP) is a clear example (Ling et al., 2015) and excellent methodologies have been developed and employed (i.e. Herrmann (2010)) for achieving this goal. On the other hand, due to the implicit necessity of having a spherical droplets for the drag model added as a source term in Eq. (1b), usually only liquid structures that are approximately spherical are detected. Furthermore, this methodology is often used as a debris removal

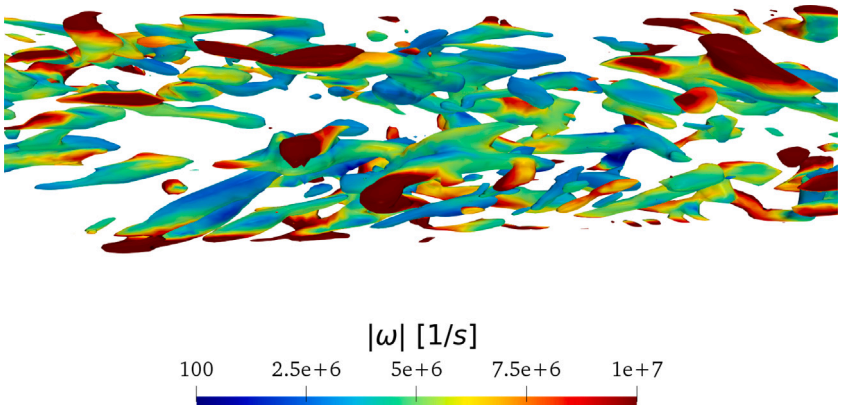

Fig. A.19. Turbulent structures captured by the Q criterion as described in Jeong et al. (1995).

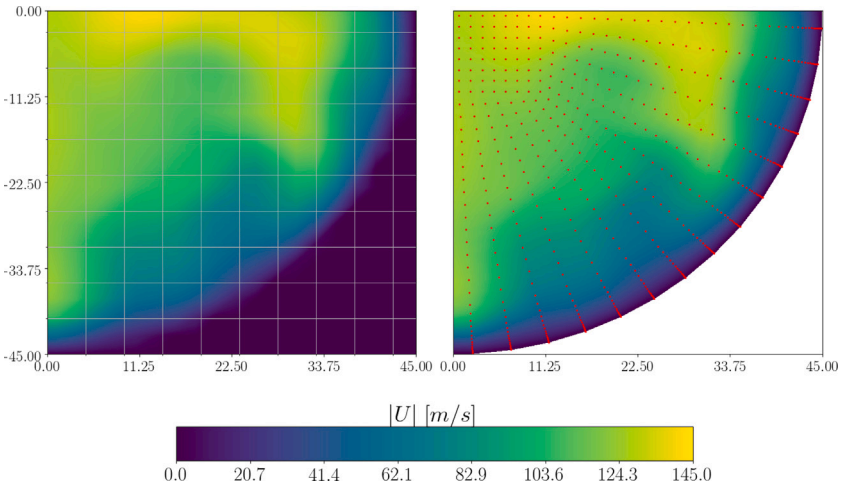

Fig. A.20. Inlet boundary condition for the MBC case. On the left the interpolated result to be fed into ParisSimulator and the mesh, on the right the LES corresponding result and the mesh points in red. All the axis are expressed in μm.

algorithm to improve the code stability (Shinjo and Umemura, 2010). In this work the whole domain is analyzed for any liquid structure of any shape and velocity. Afterwards, the liquid structures are reduced into a spheres of equivalent volume, center of mass and mean velocity to the original liquid structure. This method, while neglecting many features of the fluid structures is inherently simpler to handle. In fact, it offers a practical and easy way to compare directly the results from DNS simulations to Discrete Droplet Method (DDM) (Dukowicz, 1980). The main steps for the droplet analysis are, in sequence:

- **1- Remove the spray intact core:** in this step all the cells that are continuously attached to the nozzle outlet are removed from the computational domain. The removal procedure starts from each cell in the injection section and checks if at each successive cell in the $\hat{x}$ direction has $C \geq C_{th}$ (any cell verifying this condition is hereafter considered as full, otherwise empty). If so, the cell index is added to the collection of indexes composing the spray core and the cell color function and velocity are saved as well aside the index. The cell is then emptied, hence $C = 0$. Finally, a recursive algorithm is used to check if each cell is attached to other full cells and so on recursively until only empty cells remains in the nearby. This last iteration helps detect all the ligaments attached to the spray core and remove them as well.
- **2- Detect the droplets:** each cell of the domain is checked for $C \geq C_{th}$. If true, the recursive scanning of the cells nearby is once again called. If the code runs into a boundary or into a limit of recursive depth the liquid structure is marked for merging (which will be done at the end). Per each cell composing the droplet, only the index and the values for C and $\mathbf{u}$ are stored and are uniquely attributed to that droplet.
- **3- Droplet properties calculation:** The droplet volumetric diameter is computed as $d_v = \sqrt[3]{6V_d/\pi}$ where the droplet volume V_d is computed using the cell color function and the cell volume. The velocity and the center of mass are computed as a weighted average of the velocity components and the coordinates.

The results of the procedure described above is showed in Fig. B.21, where both the equivalent droplet and the shadowed isocontour of the VOF is showed at $t = T_t/4$.

The data displayed in the following section show the transient as well as the statistically stationary behavior. For the transient, each snapshot is analyzed every 0.5 μs until T_t and is represented against time. For the statistically stationary behavior, a snapshot is analyzed every 10 μs from T_t until $T_t + T_{ss}$ (this last sum marks the end of the simulation) and all the snapshots resulting datasets are averaged. The reason for the difference in the time sampling lays within the different goals set for each analysis. The transient analysis, in fact, relies on high frequency snapshot to try capturing the general dynamics that dictate the spray formation and the droplet generation. On the other hand, as it will be shown more clearly in the following sections (and already observed in (Shinjo and Umemura, 2011; Salvador et al., 2018)) most of the smallest droplets that are located at the spray cone periphery have already lost significant kinetic energy due to the air drag. Furthermore, most of the larger droplets (hereafter, every liquid structure will be

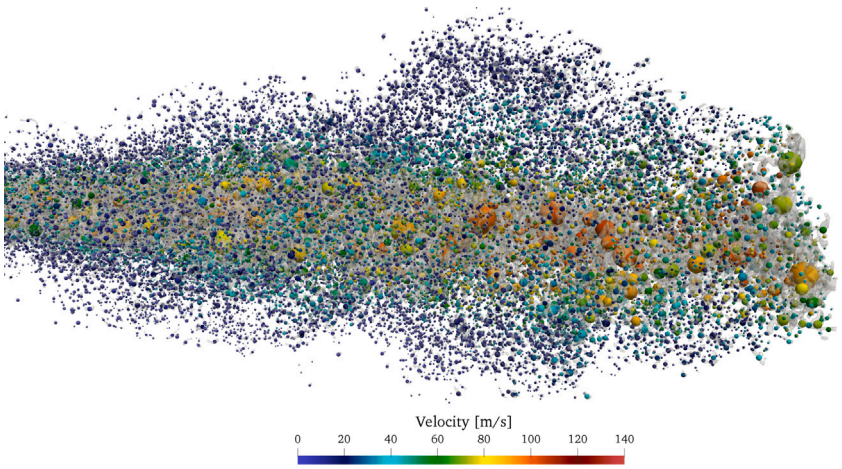

Fig. B.21. Results of the droplet detection procedure at $t = T_t/4$ with $C_{th} = 0.4$.
The equivalent droplets are colored by velocity, while the shadowed isocontour is the VOF field. (For interpretation of the references to color in this figure legend, the reader is referred to the web version of this article.)

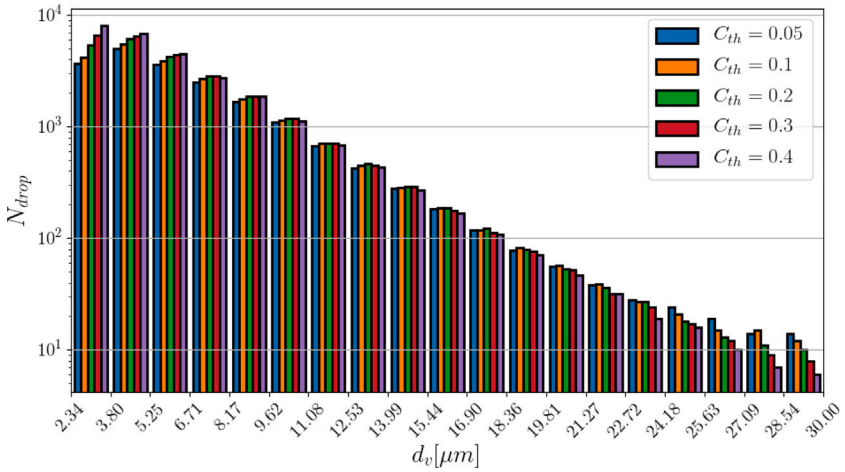

Fig. B.22. Parameterization of the C_{th} parameter during the statistically stationary part of the simulation (from T_t until $T_t + T_{ss}$).

called droplet regardless of its radius or eccentricity) are generated by the spray breakup and are advected by the main flow. In order to allow a significant time for some of these droplets to leave the domain (if such an event will occur), a significant time interval between each snapshot is required and a longer time for statistics as well. These statements will be supported by the analysis in this work.

As explained above, the only parameter that can be picked in the algorithm is C_{th}. Its value may have significant repercussions on the results and on their physical interpretation, hence it requires further analysis.

Fig. B.22 shows the effect of the value C_{th} during the droplet size distribution analysis in the statistically stationary part of the simulation. A first significant trend can be noted in the smallest range of droplets (e.g. between $d_v \in [2.34, 3.80[$). This range represents droplet of the diameter close to the simulation mesh size, dx. While these droplets are clearly meaningless physically and indicate, at best, an under-resolution of the mesh size for this type of simulation, they underline a specific behavior of the post-processing algorithm. In fact, the lower C_{th} is, the lower the number of droplets detected N_{drop}, which shows that indeed in the simulation many liquid structures are hold together by very thin liquid filaments (i.e. $C < C_{th}$), which are represented by low C in single cells connecting the droplets. Therefore, the higher C_{th}, the more these liquid structures will be divided into two (or more) droplets. This leads to an obvious underestimation of larger droplets for high values of C_{th}. In other words, low values of C_{th} accounts for ligaments on the verge of atomizing (where the low value of C compose the ligaments) as being part of larger structures, hence increasing the number of larger droplets. On the other hand, this ligaments are likely to be breaking up after few simulation timesteps, hence accounting for them as a small droplet is not strongly misleading when analyzing the results.

More importantly, Fig. B.22 highlights how there is a certain number of ranges, where $d_v \in [6.71, 22.72[$, for which N_{drop} is quite close, regardless of the value picked for C_{th}. In the authors opinion, this is actually the region where the analysis should be focused and where the most reliable data are provided. It is in fact quite clear that these droplets are in a disperse enough region of the spray so that they have more than one cell distance from any other liquid structure. Therefore, the chances of these droplets of coalescing or breaking up within short time intervals is quite reduced.

Another important effect for analyzing C_{th} carefully in DNS simulations of atomization is also that it may significantly affect the resulting distribution from a statistical standpoint. It is in fact well known that behind different probability distributions lie very different physical explanations (Villermaux, 2007). Still, this aspect is usually partially neglected when discussing numerical results and may lead to significant errors in the estimation of the statistical model used to interpret (and understand) atomization. While smaller droplets ($d_v < 4dx$) are to be considered debris, larger droplets are indeed an important part of determining the droplet size distribution. The lower likelihood of their

formation represents indeed a challenge in estimating which physical model is mostly suited to describe the process (Marmottant and Villermaux, 2004; Villermaux et al., 2004; Ling et al., 2017). As these are usually considered reliable droplets, because of the high number of grid points that defines these liquid structures, Fig. B.22 highlights how the criteria chosen for their detection has indeed a significant impact both on the accuracy of the statistical model chosen to describe these behaviors and the total droplet count. On the other hand, detection of droplets in a dispersed region (e.g. as done in Ling et al. (2017, 2019)) may limit the description of the atomization behavior, while increasing the reliability of the data analyzed. These aspects will indeed need more in-depth studies in the future.

Appendix C. Methodology for turbulence analysis in DNS

In a first place, the two most important scales in the study of turbulence are Kolmogorov space (η) and time (τ_η) scale:

$$\eta = \left(\frac{\nu^3}{\epsilon}\right)^{1/4} \tag{C.1a}$$

$$\tau_\eta = \left(\frac{\nu}{\epsilon}\right)^{1/2} \tag{C.1b}$$

Where ϵ is the energy dissipation rate. Furthermore, in the present work, the local turbulence level has been quantified using the Taylor–Reynolds number, defined as:

$$Re_\lambda = \frac{\sqrt{\langle u'^2 \rangle}\lambda}{\nu} \tag{C.2}$$

where $\langle u'^2 \rangle$ is referring to the average of the summed square of each velocity component and λ is defined as the Taylor microscale from Wilson and Hulme (1983):

$$\lambda = \sqrt{\frac{15\nu \langle u'^2 \rangle}{\epsilon}} \tag{C.3}$$

As by definition, η and τ_η are the smallest scales occurring in a turbulent flow (at least, from a kinematic standpoint), it seems natural to take them as the resolution to use in the analysis of the flow (obviously, the former spatial and the latest temporal). Many correlations have been used to estimate a-priori these scales (e.g. Pope (2001)), mostly relying on a correct estimation of the energy dissipation rate. It is therefore intuitive that the scales to be considered for the analysis are the cell size Δ and the time-step t_s used in the simulation. In other words, the sampling of the simulation results should be output each cell value, at each time-step, in lack of more accurate information.

In order to limit the amount of data required, it is important to select which information to extract. Unfortunately, no real convergent statistical study has been yet conducted on atomizing sprays. This lack of knowledge on sprays (both numerical and experimental), may be compensated by using data from single-phase jets, which are extensively documented since some of the very first analysis of energy spectra (Corrsin, 1943) and have been continuously analyzed and improved over the years (Antonia et al., 1986; Hussein et al., 1994; Sadeghi and Pollard, 2014; Craske et al., 2015).

The analogy between multiphase flow sprays and jets is quite straight forward. Both have a Gaussian velocity decay along the radial coordinate after the Near-Field is surpassed (therefore approximately when $x > 25D_n$), which is generated by shear with the calm quiescent air in the domain and is a function of the axial position; such a decay determines the velocity angle, widely characterized both experimentally and numerically in jets and sprays. An obvious consequence of the latest similarity is that, as the total momentum need to be conserved while the axial velocity decays, more momentum is transmitted in the radial direction, until the velocity eventually matches the one of the calm air (hence $u \approx 0$). As the velocity decreases radially, it may be assumed that the turbulence intensity decreases accordingly after the mixing layer. These considerations lead to the assumption that at a fixed axial distance, on each iso-radius curve (for each point located at the same radial distance from the jet centerline), the flow statistics need to be statically stationary. In other words, if we use the cylindrical coordinates (x, r, θ), fixing the first two coordinates at $x = x_p$ and $r = r_p$, $\langle u_i(\theta, t) \rangle$ and $\langle u_i'^2(\theta, t) \rangle$ are constant for each value of θ. The function $u'(\theta)$ at each time-step will obviously be a periodic function of period 2π and can be adequately defined with $\theta \in (-\pi, \pi]$.

By being $u'(\theta)$ representative of a specific turbulence level, this represents a set of data easy to compare to *Hot-Wire Anemometry* (HWA) studies of jets. In fact, the usual way to operate in this technique (Sadeghi and Pollard, 2014) is to collect first a set of time-variant data using a hot-wire sensor, then convert it to space-variant using the Taylor hypothesis:

$$\frac{\partial u}{\partial x} = \frac{1}{u}\frac{\partial u}{\partial t} \tag{C.4}$$

which is commonly known as the *Taylor frozen-turbulence hypothesis* (Taylor, 1938). While this hypothesis has not been definitively proven to be valid in free-shear flows (Tong and Warhaft, 1995), it has the inherited advantage of referring to just one point, hence only one level of turbulence (if, as in jets, such value is space dependent), consistent through the whole period of the statistic averaging. In fact, the way in which a one-dimensional spectra of the energy is usually computed in sprays is by directly applying a *Fast Fourier Transform* to the axial velocity measured along the spray centerline.

Following up on these considerations, the usage of $u'(\theta)$ is safely allowing to evaluate all turbulent structures along the azimuthal direction while providing a complete description even for sprays/jets in which no full penetration is reached.

All the considerations done lead to the conclusion that a sub-domain reaching the whole radial extension of the spray should be used. In other words, if x is the spray penetrating direction, the whole extension over y, z should be extracted at each time-step, while on the x direction only 3 points can be extracted, which are required to calculate a first order central difference for the $\partial_x u_i$ strain tensor component and should be sufficient if the mesh size is small enough.

On the other hand, the axial position for the area Ω to extract, still remains to be assessed. In order to fix that, some the knowledge from previous works of Salvador et al. (2018) and Torregrosa et al. (2020) can be used. Here it is showed clearly that once a turbulent inlet boundary condition is used, a spray axial breakup is reached and the spray intact core length is no more visible after $x/D_n > 10$. The analogy between single-phase and multiphase jets requires the presence of smooth fields for all the fluid properties for the correct determination of Eq. (C.1). For this reason, it is important to position Ω where no sharp interface can be detected stably during the whole simulation. Furthermore, a more diluted region seems more indicated for such an analysis as it is statistically impossible to have any point with a probability of 1 of having liquid during the whole averaging period. Droplet that lose momentum may stagnate in the domain, but these points are intrinsically characterized by a static velocity field, therefore out of interest for the present analysis. These considerations position Ω at $x/D_d \approx 25$.

Once Ω has been positioned, the first step is the calculation of statistics for the average fields. As a more in depth analysis of the flow average field will be done in Section 3.1, some considerations need to be done here. As we said, the goal is to define a continuous field for both density and viscosity, hence, for example, Eq. (2) could be used as a template. Let now define the field $P(x, y, z)$ which could be defined as the probability of finding liquid at any given moment in a specific location of the simulation. It could be observed that, for VOF simulations, the field P could be seen as a time average of the color-function C, but in order to maintain a general approach it is useful to consider it in terms of probability. This pseudo-fluid method has been

already used by the authors to study the turbulent behavior of sprays in Torregrosa et al. (2020), where more details on the methodology can be found.

C.1. Methodology for the spectral analysis

There are several ways of obtaining a one-dimensional spectra for a specific fluctuating velocity component. In the present work, the method by Taylor (1938) is used to calculate the autocorrelation first, and then the flow energy spectra.

The autocorrelation function is generally written as:

$$R_{ij}(\delta x, t) = \left\langle u_i'(x + \delta x, t) u_j'(x, t) \right\rangle \tag{C.5}$$

Where δx represents the lag parameter used as distances between the two correlated points in space. In the studied case, the autocorrelation could be computed over the whole range of the azimuthal coordinate θ, which is the direction over which a statistical stationary behavior can be observed. Still, as $u(\theta)$ is a periodic function, the autocorrelation should not tend to 0 asymptotically, instead should reach a peak again at $\theta = 2\pi$, as the signal returns close to its original value. For this reason, Eq. (C.5) can be rewritten in its discretized form (for a single time step):

$$R_{ij}(\xi) = \sum_{n=0}^{N_\theta - 1} u_i'(d + \Delta\theta) u_j'(\Delta\theta) \tag{C.6}$$

where N_θ is the number of element of the θ vector and ξ is the discrete distance vector (that goes linearly from 0 to $\Delta\theta(N_\theta - 1)$. By being the signal periodic, any point has $N_\theta - 1$ points on which $R_{ij}(\xi)$ can be computed, per each value of d. Therefore, a useful way to visualize the process is concatenate twice the signal $u_i'(\theta)$, but only compute $R_{ij}(\beta)$ until the point $N_\theta - 1$. Finally, any spurious frequency can be filtered by calculating the average $R_{ij}(\beta)$ over the total number of time-steps.

The non-dimensionless autocorrelation function can be used to calculate the one-dimensional spectra:

$$E_{ij}(\kappa_1) = \frac{1}{\pi} \int_0^\infty R_{ij}(\xi) e^{-i\kappa_1 \xi} d\xi \tag{C.7}$$

References

Aniszewski, W., Arrufat, T., Crialesi-Esposito, M., Dabiri, S., Fuster, D., Ling, Y., Lu, J., Malan, L., Pal, S., Scardovelli, R., et al., 2021. Parallel, robust, interface simulator (Paris). Comput. Phys. Comm. 263, 107849.

Aniszewski, W., Zaleski, S., Llor, A., Malan, L., 2019. Numerical simulations of pore isolation and competition in idealized micro-spall process. Int. J. Multi. Flow 113, 304–315. http://dx.doi.org/10.1016/j.ijmultiphaseflow.2018.10.013, URL: https://linkinghub.elsevier.com/retrieve/pii/S0301932218303082.

Antonia, R.A., Anselmet, F., Chambers, A.J., 1986. Assessment of local isotropy using measurements in a turbulent plane jet. J. Fluid Mech. 163, 365–391. http://dx.doi.org/10.1017/S0022112086002331, URL: http://www.journals.cambridge.org/abstract{_}S0022112086002331.

Benajes, J., Salvador, F.J., Carreres, M., Jaramillo, D., 2017. On the relation between the external structure and the internal characteristics in the near-nozzle field of diesel sprays. Proc. Inst. Mech. Eng. D 231, 360–371. http://dx.doi.org/10.1177/0954407016639464, URL: http://journals.sagepub.com/doi/10.1177/0954407016639464.

Biferale, L., Procaccia, I., 2005. Anisotropy in turbulent flows and in turbulent transport. http://dx.doi.org/10.1016/j.physrep.2005.04.001, arXiv:0404014.

Burton, T.M., Eaton, J.K., 2005. Fully resolved simulations of particle-turbulence interaction. J. Fluid Mech. 545, 67–111. http://dx.doi.org/10.1017/S0022112005006889.

Chehroudi, B., Talley, D., 2004. The fractal geometry of round turbulent cryogenic nitrogen jets at subcritical and supercritical pressures. At. Spray. 14.

Chorin, A.J., 1968. Numerical solution of the Navier-Stokes equations. Math. Comput. 22, 745–762. http://dx.doi.org/10.2307/2004575.

Corrsin, 1943. Spectra and Diffusion in a Round Turbulent Jet. Technical Report, URL: https://ntrs.nasa.gov/search.jsp?R=19930092091.

Craske, J., Debugne, A.L., Van Reeuwijk, M., 2015. Shear-flow dispersion in turbulent jets. J. Fluid Mech. 781, 28–51. http://dx.doi.org/10.1017/jfm.2015.417.

Davies, T.V., Batchelor, G.K., 2007. The Theory Of Homogeneous Turbulence, vol. 38. Cambridge University Press, p. 64. http://dx.doi.org/10.2307/3609796.

del Álamo, J.C., Jiménez, J., 2003. Spectra of the very large anisotropic scales in turbulent channels. Phys. Fluids 15, 41–44. http://dx.doi.org/10.1063/1.1570830.

Desjardins, O., McCaslin, J., Owkes, M., Brady, P., 2013. Direct numerical and large-eddy simulation of primary atomization in complex geometries. At. Spray. 23, 1001–1048. http://dx.doi.org/10.1615/AtomizSpr.2013007679.

Dodd, M.S., Ferrante, A., 2016. On the interaction of Taylor length scale size droplets and isotropic turbulence. J. Fluid Mech. 806, 356–412. http://dx.doi.org/10.1017/jfm.2016.550.

Dukowicz, J.K., 1980. A particle-fluid numerical model for liquid sprays. J. Comput. Phys. 35, 229–253. http://dx.doi.org/10.1016/0021-9991(80)90087-X.

Duret, B., Luret, G., Reveillon, J., Menard, T., Berlemont, A., Demoulin, F.X., 2012. DNS Analysis of turbulent mixing in two-phase flows. Int. J. Multiph. Flow 40, 93–105. http://dx.doi.org/10.1016/j.ijmultiphaseflow.2011.11.014.

Eggels, J.G.M., Unger, F., Weiss, M.H., Westerweel, J., Adrian, R.J., Friedrich, R., Nieuwstadt, F.T.M., 2006. Fully developed turbulent pipe flow: a comparison between direct numerical simulation and experiment. J. Fluid Mech. 268, 175. http://dx.doi.org/10.1017/S002211209400131X, URL: http://www.journals.cambridge.org/abstract{_}S002211209400131X.

El Khoury, G.K., Schlatter, P., Noorani, A., Fischer, P.F., Brethouwer, G., Johansson, A.V., 2013. Direct numerical simulation of turbulent pipe flow at moderately high reynolds numbers. Flow Turbul. Combust. 91, 475–495. http://dx.doi.org/10.1007/s10494-013-9482-8.

Gorokhovski, M., Herrmann, M., 2008. Modeling primary atomization. Ann. Rev. Fluid Mech. 40, 343–366. http://dx.doi.org/10.1146/annurev.fluid.40.111406.102200, URL: http://www.annualreviews.org/doi/10.1146/annurev.fluid.40.111406.102200.

Hasslberger, J., Ketterl, S., Klein, M., Chakraborty, N., 2019. Flow topologies in primary atomization of liquid jets: A direct numerical simulation analysis. J. Fluid Mech. 859, 819–838. http://dx.doi.org/10.1017/jfm.2018.845.

Herrmann, M., 2010. A parallel Eulerian interface tracking/Lagrangian point particle multi-scale coupling procedure. J. Comput. Phys. 229, 745–759. http://dx.doi.org/10.1016/j.jcp.2009.10.009.

Herrmann, M., 2011. On simulating primary atomization using the refined level set grid method. At. Spray. 21, 283–301. http://dx.doi.org/10.1615/AtomizSpr.2011002760, URL: http://www.dl.begellhouse.com/journals/6a7c7e10642258cc,4fa736af31a9c3d7,32765dc85aa6de1e.html.

Hussein, H.J., Capps, S., George, W., 1994. Velocity measurements in a high-Reynolds-number, momentum-conserving, axisymmetric, turbulent jet. J. Fluid Mech. 001, 31–75, URL: http://ceeserver.cee.cornell.edu/eac20/cee637/handouts/husseincappgeorge1994.pdf.

Issa, R.I., 1986. Solution of the implicitly discretised fluid flow equations by operator-splitting. J. Comput. Phys. 62, 40–65. http://dx.doi.org/10.1016/0021-9991(86)90099-9, arXiv:9809069v1, URL: http://www.eng.newcastle.edu.au/~jhb519/teaching/caut1/Apuntes/PID.pdf, https://linkinghub.elsevier.com/retrieve/pii/0021999186900999.

Jarrahbashi, D., Sirignano, W.A., 2014. Invited article: Vorticity dynamics for transient high-pressure liquid injection. Phys. Fluids 26, http://dx.doi.org/10.1063/1.4895781.

Jarrahbashi, D., Sirignano, W.A., Popov, P.P., Hussain, F., 2016. Early spray development at high gas density: hole, ligament and bridge formations. J. Fluid Mech. 792, 186–231. http://dx.doi.org/10.1017/jfm.2016.71, URL: http://www.journals.cambridge.org/abstract{_}S0022112016000719.

Jeong, J., Hussain, F., Jinhee, J., Fazle, H., 1995. On the identification of a vortex. J. Fluid Mech. 285, 69–94. http://dx.doi.org/10.1017/S0022112095000462.

Klein, M., Sadiki, A., Janicka, J., 2003. A digital filter based generation of inflow data for spatially developing direct numerical or large eddy simulations. J. Comput. Phys. 186, 652–665. http://dx.doi.org/10.1016/S0021-9991(03)00090-1.

Leonard, B.P., 1979. A stable and accurate convective modelling procedure based on quadratic upstream interpolation. Comput. Method. Appl. Mech. Eng. 19, 59–98. http://dx.doi.org/10.1016/0045-7825(79)90034-3, URL: https://linkinghub.elsevier.com/retrieve/pii/0045782579900343.

Ling, Y., Fuster, D., Tryggvason, G., Zaleski, S., 2019. A two-phase mixing layer between parallel gas and liquid streams: Multiphase turbulence statistics and influence of interfacial instability. J. Fluid Mech. 859, 268–307. http://dx.doi.org/10.1017/jfm.2018.825, arXiv:arXiv:1808.01996v1, URL: https://www.cambridge.org/core/product/identifier/S002211201800825X/type/journal{_}article.

Ling, Y., Fuster, D., Zaleski, S., Tryggvason, G., 2017. Spray formation in a quasiplanar gas-liquid mixing layer at moderate density ratios: A numerical closeup. Phys. Rev. Fluids 2, 014005. http://dx.doi.org/10.1103/PhysRevFluids.2.014005.

Ling, Y., Zaleski, S., Scardovelli, R., 2015. Multiscale simulation of atomization with small droplets represented by a Lagrangian point-particle model. Int. J. Multiph. Flow 76, 122–143. http://dx.doi.org/10.1016/j.ijmultiphaseflow.2015.07.002, URL: http://www.sciencedirect.com/science/article/pii/S0301932215001524.

Lucci, F., Ferrante, A., Elghobashi, S., 2010. Modulation of isotropic turbulence by particles of Taylor length-scale size. J. Fluid Mech. 650, 5–55. http://dx.doi.org/10.1017/S0022112009994022.

Marmottant, P., 2001. Atomisation d'un Jet Liquide Par Un Courant Gazeux. (Ph.D. thesis). URL: http://tel.archives-ouvertes.fr/tel-00003054.

Marmottant, P.H., Villermaux, E., 2004. On spray formation. J. Fluid Mech. 498, 73–111. http://dx.doi.org/10.1017/S0022112003006529, URL: http://www.journals.cambridge.org/abstract{_}S0022112003006529, https://www.irphe.fr/~fragmix/publis/MV2004a.pdf.

Ménard, T., Tanguy, S., Berlemont, A., 2007. Coupling level set/VOF/ghost fluid methods: Validation and application to 3D simulation of the primary break-up of a liquid jet. Int. J. Multiph. Flow 33, 510–524. http://dx.doi.org/10.1016/j.ijmultiphaseflow.2006.11.001, URL: http://www.sciencedirect.com/science/article/pii/S0301932206001832.

Milgram, J.H., 1998. Short wave damping in the simultaneous presence of a surface film and turbulence. J. Geophys. Res. Oceans 103, 15717–15727. http://dx.doi.org/10.1029/98jc01191.

Nicoud, F., Ducros, F., 1999. Subgrid-scale stress modelling based on the square of the velocity gradient tensor. Flow Turbul. Combust. 62, 183–200. http://dx.doi.org/10.1023/A:1009995426001, arXiv:arXiv:1503.01439v1.

Park, G.I., Bassenne, M., Urzay, J., Moin, P., 2017. A simple dynamic subgrid-scale model for les of particle-laden turbulence. Phys. Rev. Fluids 2, 1–20. http://dx.doi.org/10.1103/PhysRevFluids.2.044301.

Pitsch, H., Desjardins, O., 2010. Detailed numerical investigation of turbulent atomization of liquid jets. At. Spray. 20, 311–336. http://dx.doi.org/10.1615/atomizspr.v20.i4.40.

Pope, S.B., 2001. Turbulent flows. http://dx.doi.org/10.1088/0957-0233/12/11/705.

Popinet, S., 2009. An accurate adaptive solver for surface-tension-driven interfacial flows. J. Comput. Phys. 228, 5838–5866. http://dx.doi.org/10.1016/j.jcp.2009.04.042.

Prakash, V.N., Martínez Mercado, J., Van Wijngaarden, L., Mancilla, E., Tagawa, Y., Lohse, D., Sun, C., 2016. Energy spectra in turbulent bubbly flows. J. Fluid Mech. 791, 174–190. http://dx.doi.org/10.1017/jfm.2016.49, arXiv:1307.6252.

Rogallo, R.S., 1981. Numerical experiments in homogeneous turbulence numerical experiments in homogeneous turbulence. Nasa Technical Memorandum 93.

Rosti, M.E., Ge, Z., Jain, S.S., Dodd, M.S., Brandt, L., 2020. Droplets in homogeneous shear turbulence. J. Fluid Mech. 876, 962–984. http://dx.doi.org/10.1017/jfm.2019.581.

Sadeghi, H., Pollard, A., 2014. Axial velocity spectra scaling in a round, free jet. In: Proceeding Of THMT-12. Proceedings Of The Seventh International Symposium On Turbulence, Heat And Mass Transfer Palermo, Italy, 24-27 September, 2012, 2014, p. 11, 10.1615/ichmt.2012.procsevintsympturbheattransfpal.1220, URL: http://www.dl.begellhouse.com/references/1bb331655c289a0a,7c69ce3452e09525,2eab79c17f0305b5.html.

Sahu, S., Hardalupas, Y., Taylor, A.M., 2016. Droplet-turbulence interaction in a confined polydispersed spray: Effect of turbulence on droplet dispersion. J. Fluid Mech. 794, 267–309. http://dx.doi.org/10.1017/jfm.2016.169.

Salvador, F., Ruiz, S., Crialesi-Esposito, M., Blanquer, I., 2018. Analysis on the effects of turbulent inflow conditions on spray primary atomization in the near-field by direct numerical simulation. Int. J. Multiph. Flow 102, 49–63. http://dx.doi.org/10.1016/j.ijmultiphaseflow.2018.01.019, URL: http://linkinghub.elsevier.com/retrieve/pii/S0301932217305037.

Scardovelli, R., Zaleski, S., 1999. Direct numerical simulation of free-surface and interfacial flow. Ann. Rev. Fluid Mech. 31, 567–603. http://dx.doi.org/10.1146/annurev.fluid.31.1.567, URL: http://www.annualreviews.org/doi/10.1146/annurev.fluid.31.1.567.

Shinjo, J., Umemura, A., 2010. Simulation of liquid jet primary breakup: Dynamics of ligament and droplet formation. Int. J. Multiph. Flow 36, 513–532. http://dx.doi.org/10.1016/j.ijmultiphaseflow.2010.03.008, URL: http://linkinghub.elsevier.com/retrieve/pii/S0301932210000637.

Shinjo, J., Umemura, A., 2011. Detailed simulation of primary atomization mechanisms in Diesel jet sprays (isolated identification of liquid jet tip effects). Proc. Combust. Inst. 33, 2089–2097. http://dx.doi.org/10.1016/j.proci.2010.07.006, URL: http://linkinghub.elsevier.com/retrieve/pii/S154074891000235X.

Subramaniam, S., 2000. Statistical representation of a spray as a point process. Phys. Fluids 12, 2413–2431. http://dx.doi.org/10.1063/1.1288266.

Sundaram, S., Collins, L.R., 1999. A numerical study of the modulation of isotropic turbulence by suspended particles. J. Fluid Mech. 379, 105–143. http://dx.doi.org/10.1017/S0022112098003073.

Sussman, M., 1994. A level set approach for computing solutions to incompressible two-phase flow. J. Comput. Phys. 114, 146–159. http://dx.doi.org/10.1006/jcph.1994.1155, arXiv:1994, URL: http://linkinghub.elsevier.com/retrieve/pii/S0021999184711557.

Taylor, G.I., 1938. The spectrum of turbulence. Proc. R. Soc. A 164, 476–490. http://dx.doi.org/10.1098/rspa.1938.0032, arXiv:1108.0910, URL: http://rspa.royalsocietypublishing.org/cgi/doi/10.1098/rspa.1983.0054, http://www.royalsocietypublishing.org/doi/10.1098/rspa.1938.0032.

Tong, C., Warhaft, Z., 1995. Passive scalar dispersion and mixing in a turbulent jet. J. Fluid Mech. 292, 1–38. http://dx.doi.org/10.1017/S0022112095001418, URL: http://www.journals.cambridge.org/abstract{_}S0022112095001418.

Torregrosa, A.J., Payri, R., Javier Salvador, F., Crialesi-Esposito, M., 2020. Study of turbulence in atomizing liquid jets. Int. J. Multiph. Flow 129, http://dx.doi.org/10.1016/j.ijmultiphaseflow.2020.103328.

Tryggvason, G., Bunner, B., Esmaeeli, A., Juric, D., Al-Rawahi, N., Tauber, W., Han, J., Nas, S., Jan, Y.J., 2001. A front-tracking method for the computations of multiphase flow. J. Comput. Phys. 169, 708–759. http://dx.doi.org/10.1006/jcph.2001.6726.

Tryggvason, G., Scardovelli, R., Zaleski, S., 2011. Direct Numerical Simulations of Gas–Liquid Multiphase Flows. Cambridge University Press.

Tsuji, Y., 2003. Large-scale anisotropy effect on small-scale statistics over rough wall turbulent boundary layers. Phys. Fluids 15, 3816–3828. http://dx.doi.org/10.1063/1.1622395.

Villermaux, E., 2007. Fragmentation. Ann. Rev. Fluid Mech. 39, 419–446. http://dx.doi.org/10.1146/annurev.fluid.39.050905.110214, http://www.annualreviews.org/doi/10.1146/annurev.fluid.39.050905.110214, https://linkinghub.elsevier.com/retrieve/pii/S0378437106005097.

Villermaux, E., Marmottant, P., Duplat, J., 2004. Ligament-mediated spray formation. Phys. Rev. Lett. 92, 074501. http://dx.doi.org/10.1103/PhysRevLett.92.074501.

Wilson, S.D.R., Hulme, A., 1983. The effect of bubbles attached to an electrode on electrical resistance and dissolved gas concentration. Proc. R. Soc. A 387, 133–146. http://dx.doi.org/10.1098/rspa.1983.0054, URL: http://rspa.royalsocietypublishing.org/cgi/doi/10.1098/rspa.1983.0054.

Wu, X., Moin, P., 2008. A Direct Numerical Simulation Study On The Mean Velocity Characteristics In Turbulent Pipe Flow, vol. 608. http://dx.doi.org/10.1017/S0022112008002085.

Zandian, A., Sirignano, W.A., Hussain, F., 2018. Understanding liquid-jet atomization cascades via vortex dynamics. J. Fluid Mech. 843, 293–354. http://dx.doi.org/10.1017/jfm.2018.113, arXiv:1706.03742.